AN ABSTRACT OF THE THESIS OF

Patrick Thomas Reardon for the degree of Master of Science

in Nuclear Engineering presented on May 17, 1983

Title: A Two-Dimensional Analysis of Porosity Effects on the Thermal Conductivity of Ceramic Nuclear Fuels

Abstract Approved: Redacted for Privacy

K. L. Peddicord

Heat transfer in ceramic nuclear fuels is complicated by the presence of entrained porosity. The characteristic heat transfer is an important factor in the design and operation of reactor cores. Initially, porosity is uniformly distributed and is primarily due to fabrication effects. Later, fission gases coalesce and pellets crack to introduce additional porosity. A porosity correction factor is typically defined which modifies the thermal conductivity of either the 100% dense solid, or some other reference density to account for the presence of the porosity in heat transfer calculations.

Early analytical approaches were primarily one-dimensional and would not allow heat flow around a pore. The first to allow for multi-dimensional heat flow was Cunningham, who solved the heat conduction equation in three dimensions, finding the temperature field throughout a unit cell which consisted of a single sphere in a cube. The ratio of effective conductivity to the conductivity of 100% dense material is given by

$$f(p) = e^{-2.14p} \text{ for } 0 \leq p \leq 0.3$$

$$f(p) = 0.92 - 1.34p \text{ for } 0.3 \leq p \leq 0.5.$$

The purpose of this work was to assess the method of Cunningham by performing a two-dimensional analytical study which was then compared to idealized measurements using an electrical analog for heat flow.

These measurements were made using resistance paper, and a "temperature" field was found throughout the unit cell. By summing the resistance to heat flow, and averaging over the cross-sectional area of the unit cell, porosity correction formulas were determined. For further confirmation, the unit cell was modeled using a finite element code (TAP-A) developed for heat transfer calculations for the Fast Flux Test Facility, located at Hanford, Washington.

All three two-dimensional methods gave results which support the Cunningham methodology. The two-dimensional analysis and that of Cunningham consistently lie within a few percent. By contrast, the previous one-dimensional approaches yielded inadequate results when compared to the electrical analog. Cases were examined using the electrical analog where pores were distributed throughout the unit cell in a normal random fashion centered at the middle of the unit cell. As before, the two-dimensional analysis and that of Cunningham closely predicted the experimentally determined effective conductivity.

A TWO-DIMENSIONAL ANALYSIS OF POROSITY EFFECTS ON THE THERMAL CONDUCTIVITY OF CERAMIC NUCLEAR FUELS

by

Patrick Thomas Reardon

A THESIS

submitted to

Oregon State University

in partial fulfillment of
the requirements for the
degree of

Master of Science

Completed May 17, 1983

Commencement June 1984

APPROVED:

Redacted for Privacy

Professor of Nuclear Engineering

Redacted for Privacy

Head of Department of Nuclear Engineering

Redacted for Privacy

Dean of Graduate School

Date thesis is presented May 17, 1983

Typed by Pat Oliver for Patrick Thomas Reardon

TABLE OF CONTENTS

LIST OF FIGURES

LIST OF TABLES

A TWO-DIMENSIONAL ANALYSIS OF POROSITY EFFECTS ON THE THERMAL CONDUCTIVITY OF CERAMIC NUCLEAR FUELS

I. INTRODUCTION

Heat transfer in ceramic nuclear fuels is complicated by the presence of entrained porosity. In fresh fuel, the porosity is uniformly distributed with a range of pore sizes, and is due primarily to fabrication effects. Typically, this fabrication porosity is on the order of four to five percent by volume. During irradiation, fission gases, primarily xenon and krypton, are formed which coalesce into bubbles, adding to the fuel porosity. Pellet cracking and relocation followed by sintering can also introduce additional porosity.

To account for the presence of the porosity in heat transfer calculations, a porosity correction factor is typically defined which modifies the thermal conductivity of either the 100% dense solid, or some other reference density. This correction factor has the form

$$K_p = K_{ref} \times f(p)$$

where K_p = conductivity of the porous material
K_{ref} = conductivity of the reference density material (usually 100%)
$f(p)$ = porosity correction factor for fractional porosity, p.

Several approaches have been taken to determine this factor. These include empirical methods resulting from experimentation, and analytical methods. Among the first suggestions for a porosity correction formula was that of Loeb in which the conductivity is modified by the ratio of the actual density to the maximum theoretical density (1). This is expressed as

$$f(p) = 1 - p$$

This expression proved unsatisfactory when compared to experimental data, and led to the modified Loeb formula (1). This expression is as follows:

$$f(p) = 1 - \alpha p$$

where α varies between 1.7 and 2.5. Another empirical expression is given by Maxwell-Eucken (2) as

$$f(p) = \frac{1 - p}{1 + \beta p}$$

where β = 1.0 for carbide fuels
= 0.5 for oxide fuels greater than 90% theoretical density
= 0.7 for oxide fuels less than 90% theoretical density.

Kampf and Karsten developed an analytical correction in which a cubical pore is located in the center of a cube of material (3). Heat flow is in one direction only with no heat flow around the pore. By summing the resistance to heat flow, and averaging over the cross sectional area of the unit cell, the porosity correction formula obtained is

$$f(p) = 1 - p^{2/3}.$$

This approach was used for a spherical pore in the center of a cubical cell by Peddicord (4) to give the analytical porosity correction formula

$$f(p) = 1 - \left[\frac{3\pi^{1/2}}{4} \right]^{2/3} p.$$

The next step in analytical solutions was to allow for multidimensional heat flow. Cunningham (5) solved the heat conduction equation in three dimensions finding the temperature field throughout the unit cell. The unit cell consisted of a single sphere in a cube. The heat flux entering and leaving the unit cell was determined, and an effective

conductivity found. This effective conductivity was then compared to the conductivity of 100% dense material generating a ratio dependent on porosity, and used as a correction formula. The resulting expression is

$$f(p) = e^{-2.14p} \text{ for } 0 \leq p \leq 0.3$$

and $$f(p) = 0.92 - 1.34p \text{ for } 0.3 \leq p \leq 0.5.$$

The empirical methods derived from experimental data have proven to be valid to only about 12% porosity. In actual fuel pellets, porosities of 35 to 50% are achieved. The analytical method developed by Cunningham was the first to allow for multidimensional heat flow. Previous analytical methods were one dimensional, and allowed for no heat flow around the pore. By ignoring multidimensional heat flow, the effects of porosity are usually overestimated.

The purpose of this work is to assess the method of Cunningham by undertaking a two-dimensional analytical study which could then be compared to idealized measurements using an electrical analog for heat flow. An effective conductivity determined as a ratio will produce a conductivity correction formula as a function of porosity. For direct comparison, one can make measurements using resistance paper, determining the value of the temperature at any point in the system. If the two-dimensional analytical expression is supported, one gains greater confidence in that generated for the three-dimensional case.

The scope of this work will be to develop an analytical temperature profile for the entire unit cell, and develop a porosity correction formula based on this analytical solution. After completion of this portion of the work, an electrical analog using resistance paper will be used to access the solutions obtained in the analytical approach.

As further confirmation, the analytical approach will be simulated using a finite element code developed by Westinghouse called TAP-A (6). TAP-A was the code used to do much of the initial heat transfer calculations for the Fast Flux Test Facility at Hanford, Washington.

II. THE UNIT CELL AND BOUNDARY CONDITIONS

The problem under consideration is an array of rectangular parallelepipeds with cylinderical pores as shown in Figure 1. The pores are considered to be of uniform diameter, and consist of a homogenous material with constant properties. The second material is also assumed to have constant properties.

The approach to be used in this paper is to slice a two-dimensional cross section through the parallelepiped, and preserve the boundary conditions of the solid in the cross section. The cross section is shown in Figure 2. On the upper and lower edges, it is assumed that the temperature at all points is known. Due to the symmetry of the cross section, it may be assumed there is no heat transfer between adjacent cells (adiabatic sides), and all heat transfer occurs perpendicular to the top and bottom edges.

One further division gives the unit cell to be considered. Since the temperature profile in the full cell of Figure 2 is known along the top and bottom edge, and are different, the full height of the cell is preserved. A line of symmetry exists down the center of the cell as shown in Figure 3. All heat flow will be between the top and bottom edges, and none between adjacent cells. This, by definition, makes both edges adiabatic.

This problem is to be treated in cylindrical geometry. Any point in the unit cell can be described by the coordinates (r,θ) where r is the distance from the origin to the point, and θ is the angle between the y-axis and the line to the point. This is shown in Figure 4.

The governing steady state heat conduction equation for this system is the Laplace Equation given by:

$$\frac{1}{r}\frac{\partial}{\partial r}\left[r\frac{\partial}{\partial r}T(r,\theta)\right] + \frac{1}{r^2}\frac{\partial^2}{\partial \theta^2}T(r,\theta) = 0. \qquad (II\text{-}1)$$

At this point, it will be helpful to discuss the various interface and boundary conditions that must be satisfied. Referring to Figure 4, one sees the following:

(1) Continuity of temperature at the region interface

$$T^{(1)}(\rho,\theta) = T^{(2)}(\rho,\theta) \qquad \text{(II-2)}$$

where ρ is the radius of the pore.

(2) Continuity of heat flux at the region interface

$$-K^{(1)} \frac{\partial T^{(1)}}{\partial r}\bigg|_{r=\rho} = -K^{(2)} \frac{\partial T^{(2)}}{\partial r}\bigg|_{r=\rho}. \qquad \text{(II-3)}$$

(3) Finite temperature at the cell center

$$\lim_{r \to 0} T^{(1)} = \text{finite}. \qquad \text{(II-4)}$$

The unit cell is bounded by three distinct edges. The top edge, from $0 \leq \theta \leq \frac{\pi}{4}$, the temperature at any point is known and given by $T(r,\theta)=1$, where $r = \frac{L}{2\cos\theta}$. Likewise on the bottom edge, from $\frac{3\pi}{4} \leq \theta \leq \pi$, the temperature at any point is known and given by $T(r,\theta) = 0$, where $r = -\frac{L}{2\cos\theta}$. The conditions of the adiabatic edges that are somewhat more involved for this condition require that the component of the heat flux vector normal to the edge be zero. This is given by

$$\hat{e}_x \cdot q''(r,\theta)\bigg|_{r=\frac{L}{2\sin\theta}} = 0 \text{ for } \frac{\pi}{4} \leq \theta \leq \frac{3\pi}{4} \qquad \text{(II-5)}$$

where $q''(r,\theta) = -K^{(2)}\nabla T^{(2)}(r,\theta)$ = heat flux

$\hat{e}_x$ = unit vector in the x-direction.

This condition can be shown (Appendix B) to reduce to the following:

$$\sin\theta \frac{\partial}{\partial r} T^{(2)}(r,\theta) + \cos\theta \frac{1}{r} \frac{\partial}{\partial \theta} T^{(2)}(r,\theta) = 0. \qquad \text{(II-6)}$$

FIGURE 1.
THREE-DIMENSIONAL PORE ARRAY

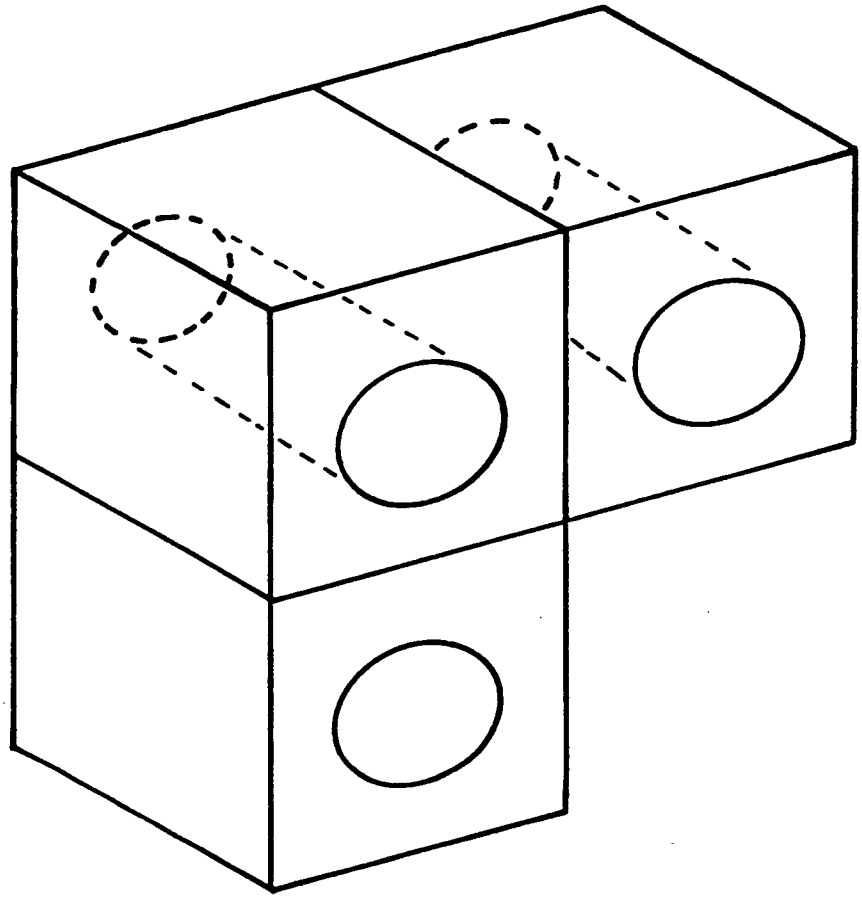

FIGURE 2.
CROSS-SECTIONAL AREA

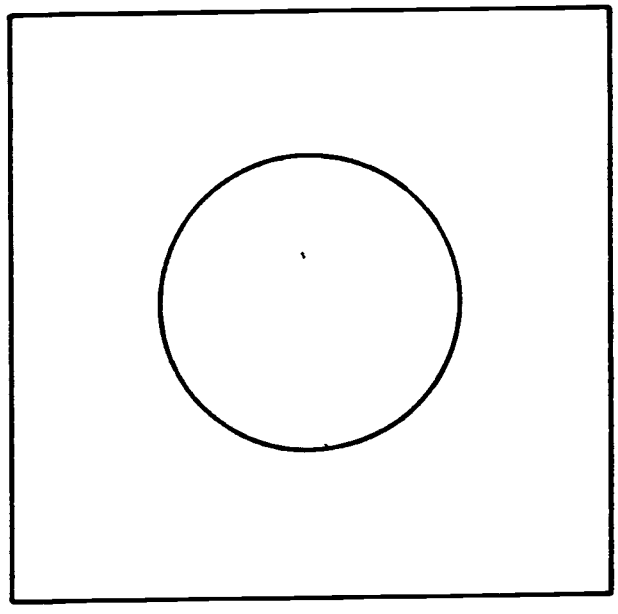

FIGURE 3.
UNIT CELL CONSIDERED

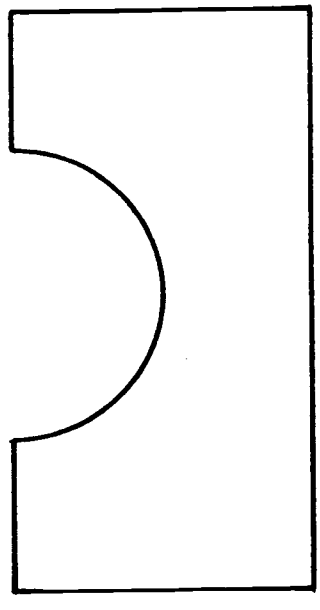

FIGURE 4.
UNIT CELL WITH BOUNDARY CONDITIONS DEFINED

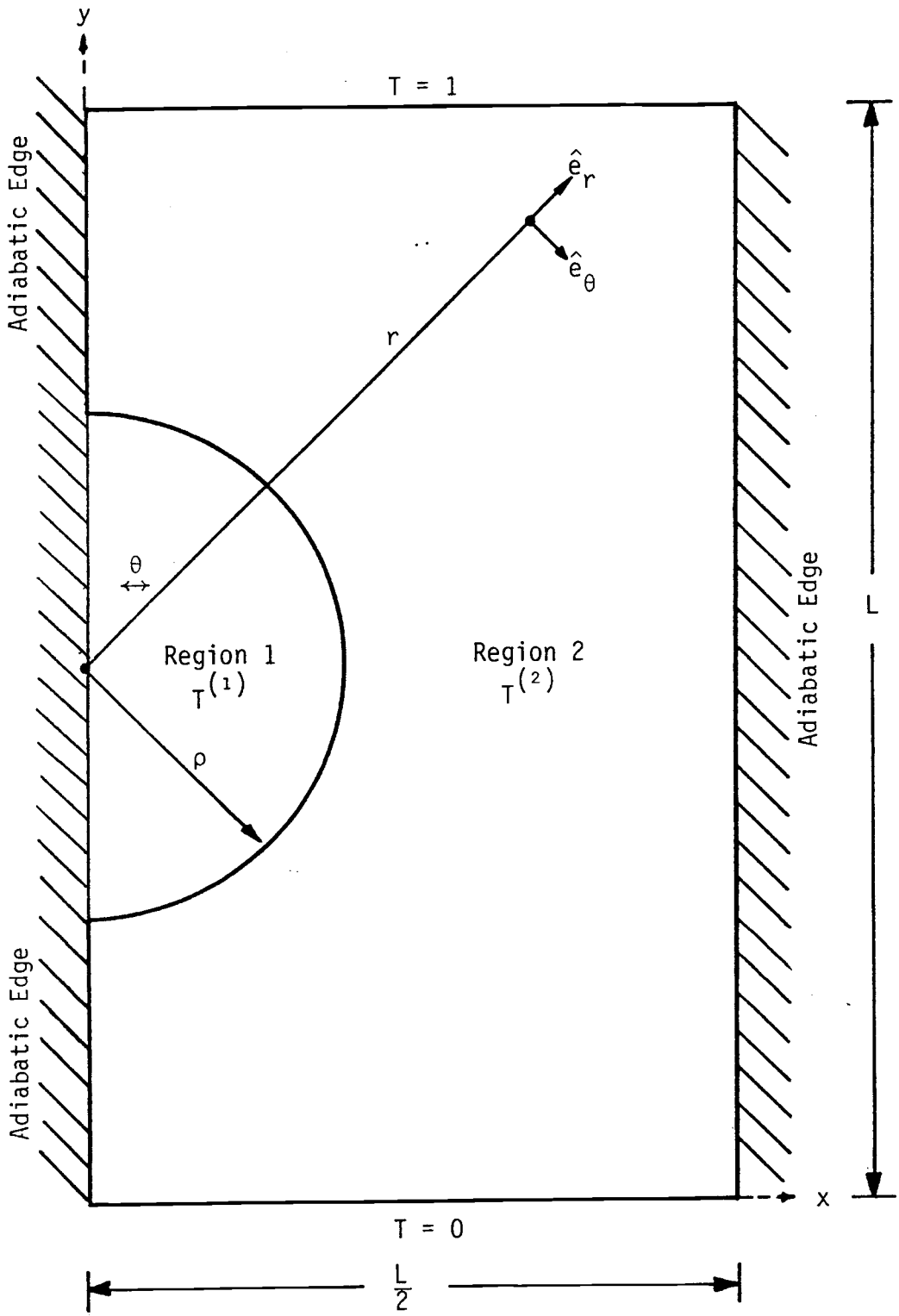

III. DEVELOPMENT OF THE SOLUTIONS

A. The Analytical Solution

The analytical solution is found by solving a linear system of partial differential equations for systems of constant properties. The general solution will consist of the complete solution of the homogeneous differential equation plus one particular solution of the inhomogeneous equation. The arbitrary coefficients to the homogeneous equation are determined by the boundary conditions.

The general solution to the governing differential equation, Equation (II-1), can be shown (Appendix A) to have the general solution form in each region as follows:

$$T(r,\theta) = Ao + Bo \ln r + \sum_{n=1}^{\infty} [An\ r^{n} + Bn\ r^{-n}]\ \cos(n\theta). \quad \text{(III-1)}$$

To this equation the boundary conditions must be applied.

In region 1, the finite temperatures everywhere in the cell condition implies all the coefficients, B, must be zero. This leaves

$$T^{(1)}(r,\theta) = Ao + \sum_{n=1}^{\infty} An\ r^{n} \cos(n\theta). \quad \text{(III-2)}$$

In region 2, the solution is as follows:

$$T^{(2)}(r,\theta) = Co + Do \ln r + \sum_{n=1}^{\infty} [Cn\ r^{n} + Dn\ r^{-n}] \cos(n\theta). \quad \text{(III-3)}$$

To solve for the remaining coefficients A_o, A_n, C_o, C_n, D_o, and D_n, two properties of the $\cos(n\theta)$ are used. The orthogonality properties are:

Property 1: $\int_0^{\pi} \cos(n\theta)d\theta = \sin(n\theta)\Big|_0^{\pi} = 0$

Property 2: $\int_0^{\pi} \cos(n\theta)\cos(m\theta)d\theta = \begin{cases} \frac{\pi}{2} & \text{for } n=m \\ 0 & \text{otherwise.} \end{cases}$

Applying the interface condition of temperature continuity, $T^{(1)}(\rho,\theta) = T^{(2)}(\rho,\theta)$ yields

$$Ao + \sum_{n=1}^{\infty} An\ \rho^n \cos(n\theta) = Co + Do\ \ln \rho + \sum_{n=1}^{\infty} [Cn\ \rho^n + Dn\ \rho^{-n}] \cos(n\theta). \tag{III-4}$$

Integrating over all θ in the unit cell gives

$$\int_0^{\pi} \Big(Ao + \sum_{n=1}^{\infty} An\ \rho^n \cos(n\theta) \Big) d\theta = \int_0^{\pi} \Big(Co + Do\ \ln \rho + \sum_{n=1}^{\infty} [Cn\ \rho^n + Dn\ \rho^{-n}] \cos(n\theta) \Big) d\theta. \tag{III-5}$$

Applying Property 1 eliminates all terms except

$$Ao\theta \Big|_0^{\pi} = Co\theta \Big|_0^{\pi} + (Do\ \ln \rho)\theta \Big|_0^{\pi}.$$

This reduces to

$$Ao = Co + Do\ \ln \rho. \tag{III-6}$$

Multiplying both sides of equation (III-4) by $\cos(m\theta)$ and integrating over all θ in the unit cell gives

$$\int_0^{\pi} \Big(Ao \cos(m\theta) + \sum_{n=1}^{\infty} An\ \rho^n \cos(n\theta) \cos(m\theta) \Big) d\theta =$$

$$\int_0^{\pi} \Big(Co \cos(m\theta) + (D_o \ln \rho) \cos(m\theta) + \sum_{n=1}^{\infty} [Cn\ \rho^n + Dn\ \rho^{-n}] \cos(n\theta) \cos(m\theta) \Big) d\theta. \tag{III-7}$$

Applying Property 1, the leading terms on both sides are eliminated and the only nonzero term occurs when n=m in the summation. Cancelling gives

$$Am\ \rho^m = Cm\ \rho^m + Dm\ \rho^{-m}. \tag{III-8}$$

Now consider the second interface condition, i.e., continuity of heat flux at $r = \rho$. This condition is

$$-K^{(1)} \left.\frac{\partial T^{(1)}}{\partial r}\right|_{r=\rho} = -K^{(2)} \left.\frac{\partial T^{(2)}}{\partial r}\right|_{r=\rho}.$$

To analyze this condition, it is necessary to evaluate, in each region, the partial derivative. In Region 1, the temperature field is given by Equation (III-2) which leads to

$$\frac{\partial T^{(1)}}{\partial r} = \frac{\partial}{\partial r}\left[Ao + \sum_{n=1}^{\infty} An\, r^n \cos(n\theta)\right].$$

This expression reduces to

$$\frac{\partial T^{(1)}}{\partial r} = \sum_{n=1}^{\infty} nAn\, r^{n-1} \cos(n\theta). \qquad \text{(III-9)}$$

Similarly in Region 2, from Equation (III-3)

$$\frac{\partial T^{(2)}}{\partial r} = \frac{\partial}{\partial r}\left[Co + Do \ln r + \sum_{n=1}^{\infty} [Cn\, r^n + Dn\, r^{-n}] \cos(n\theta)\right].$$

This expression reduces to

$$\frac{\partial T^{(2)}}{\partial r} = \frac{Do}{r} + \sum_{n=1}^{\infty} \left[nCn\, r^{n-1} - nDn\, r^{-n-1}\right] \cos(n\theta). \qquad \text{(III-10)}$$

Setting Equations (III-9) and (III-10) equal, and integrating over all θ in the unit cell gives

$$-K^{(1)} \int_0^{\pi} \left[\sum_{n=1}^{\infty} nAn\, \rho^{n-1} \cos(n\theta) \right] d\theta = -K^{(2)} \int_0^{\pi} \left[\frac{Do}{\rho} + \sum_{n=1}^{\infty} \left(nCn\, \rho^{n-1} - nDn\, \rho^{-n-1} \right) \cos(n\theta) \right] d\theta. \qquad \text{(III-11)}$$

Applying Property 1, the left-hand side is zero, and all but the leading term on the right-hand side is zero. Simplifying leaves

$$0 = -K^{(2)} \frac{Do}{\rho} \theta \Big|_{o}^{\pi} .$$

Since -K, ρ, and π are not zero, this implies that $D_o = 0$.

As before, multiply both sides of equation (III-11) by cos(mθ) and integrate over the entire interface. This gives

$$-K^{(1)} \int_{o}^{\pi} \left[\sum_{n=1}^{\infty} nAn\ \rho^{n-1} \cos(n\theta)(\cos m\theta) \right] d\theta = -K^{(2)} \int_{o}^{\pi} \left[\frac{Do}{\rho} + \sum_{n=1}^{\infty} \left(nCn\ \rho^{n-1} - nDn\ \rho^{-n-1} \right) \cos(n\theta) \right] \cos(m\theta) d\theta. \qquad \text{(III-12)}$$

Making use of Properties 1 and 2 eliminates the $\frac{Do}{\rho}$ term and is everywhere zero, except when n=m. This gives

$$-K^{(1)}\ mAm\ \rho^{m-1} \left(\frac{\pi}{2}\right) = -K^{(2)} \left(mCm\ \rho^{m-1} - mDm\ \rho^{-m-1} \right) \frac{\pi}{2} .$$

Reducing gives

$$-K^{(1)}\ Am\ \rho^{m-1} = -K^{(2)} \left(Cm\ \rho^{m-1} - Dm\ \rho^{-m-1} \right) . \qquad \text{(III-13)}$$

It is now necessary to consider the conditions along the cell boundary in Region 2. Along the top edge, it is assumed that $T(r,\theta)$ is known everywhere and is set to a constant. This is shown as follows:

$$T^{(2)}\ (r,\theta) = 1 \text{ for } 0 \leq \theta \leq \frac{\pi}{4} . \qquad \text{(III-14)}$$

This gives, from equation (III-3)

$$1 = Co + \sum_{n=1}^{\infty} \left(Cn\ r^{n} + Dn\ r^{-n} \right) \cos(n\theta). \qquad \text{(III-15)}$$

Along the top edge, $r = \frac{L}{2\cos\theta}$. When this is substituted into equation (III-15)the result is only a function of θ in the range $0 \geq \theta \geq \frac{\pi}{4}$

$$1 = Co + \sum_{n=1}^{\infty} \left(Cn\left(\frac{L}{2\cos\theta}\right)^{n} + Dn\left(\frac{L}{2\cos\theta}\right)^{-n} \right) \cos(n\theta). \qquad \text{(III-16)}$$

Similarly, along the bottom edge $T(r,\theta)$ is known and assumed to be a constant value which is less than the condition on the upper edge. This is necessary to cause a heat flow between the upper and lower edges.

$$T^{(2)}(r,\theta) = 0 \text{ for } \frac{3\pi}{4} \leq \theta \leq \pi. \qquad \text{(III-17)}$$

Noting the radius along this edge is given by $r = -\frac{L}{2\cos\theta}$ and combining into equation (III-3) gives an expression in terms of θ as follows:

$$0 = Co + \sum_{n=1}^{\infty} \left(Cn\left(-\frac{L}{2\cos\theta}\right)^{n} + Dn\left(-\frac{L}{2\cos\theta}\right)^{-n} \right) \cos(n\theta). \qquad \text{(III-18)}$$

The adiabatic side condition is a bit more complicated. It was shown that the adiabatic condition can be written as

$$\sin\theta \frac{\partial}{\partial r} T^{(2)}(r,\theta) + \frac{\cos\theta}{r} \frac{\partial}{\partial \theta} T^{(2)}(r,\theta) = 0. \qquad \text{(III-19)}$$

It is again necessary to evalute the partial derivatives.

$$\frac{\partial}{\partial r} T^{(2)}(r,\theta) = \frac{\partial}{\partial r} \sum_{n=1}^{\infty} \left(nCn\, r^{n-1} \cos(n\theta) - nDn\, r^{-n-1} \cos(n\theta) \right) \qquad \text{(III-20)}$$

Noting that the outside boundary between $\frac{\pi}{4} \leq \theta \leq \frac{3\pi}{4}$ is given by $r = \frac{L}{2\sin\theta}$, and substituting in gives

$$\frac{\partial}{\partial r} T^{(2)}(r,\theta) = \sum_{n=1}^{\infty} \left(nCn\left(\frac{L}{2\sin\theta}\right)^{n-1} \cos(n\theta) - nDn\left(\frac{L}{2\sin\theta}\right)^{-n-1} \cos(n\theta) \right). \qquad \text{(III-21)}$$

For the other partial derivative the same procedure is used. This gives

$$\frac{\partial}{\partial\theta} T^{(2)}(r,\theta) = \frac{\partial}{\partial\theta} [Co + \sum_{n=1}^{\infty}\Big(Cn\ r^{n} \cos(n\theta) + Dn\ r^{-n} \cos(n\theta)\Big)]$$

hence,

$$\frac{\partial}{\partial\theta} T^{(2)}(r,\theta) = \sum_{n=1}^{\infty} \Big(-nCn\ r^{n} \sin(n\theta) - nDn\ r^{-n} \sin(n\theta)\Big). \quad \text{(III-22)}$$

Again substituting $r = \left(\frac{L}{2\sin}\right)$ gives

$$\frac{\partial}{\partial\theta} T^{(2)}(r,\theta) = \sum_{n=1}^{\infty} \Big(-nCn\Big(\frac{L}{2\sin\theta}\Big)^{n} \sin(n\theta) - nDn\Big(\frac{L}{2\sin\theta}\Big)^{-n} \sin(n\theta)\Big). \quad \text{(III-23)}$$

Now substituting equations (III-21) and (III-23) into equation (III-19) yields

$$\sin\theta \left\{ \sum_{n=1}^{\infty} \Big(nCn\Big(\frac{L}{2\sin\theta}\Big)^{n-1} \cos(n\theta) - nDn\Big(\frac{L}{2\sin\theta}\Big)^{-n-1} \cos(n\theta)\Big) \right\} +$$

$$\frac{\cos\theta}{r} \left\{ \sum_{n=1}^{\infty} \Big(-nCn\Big(\frac{L}{2\sin\theta}\Big)^{n} \sin(n\theta) - nDn\Big(\frac{L}{2\sin\theta}\Big)^{-n} \sin(\theta)\Big) \right\} = 0.$$

Combining terms and simplifying gives

$$\sum_{n=1}^{\infty} \Big(nCn\Big(\frac{L}{2\sin\theta}\Big)^{n-1} \Big\{ \sin\theta \cos(n\theta) - \cos\theta \sin(n\theta) \Big\} - nDn\Big(\frac{L}{2\sin\theta}\Big)^{-n-1}$$

$$\Big\{\sin\theta \cos(n\theta) + \cos\theta \sin(n\theta)\Big\}\Big) = 0. \quad \text{(III-24)}$$

The top, side, and bottom boundary conditions are all now in a similar format. This is shown on the following page.

$$Co + \sum_{n=1}^{\infty}\left\{Cn\left(\frac{L}{2\cos\theta}\right)^{n}\cos(n\theta) + Dn\left(\frac{L}{2\cos\theta}\right)^{-n}\right\}\cos(n\theta) = 1$$

$$\text{for } 0 \leq \theta \leq \frac{\pi}{4}$$

$$\sum_{n=1}^{\infty}\left(n\,Cn\left(\frac{L}{2\sin\theta}\right)^{n-1}\left\{\sin\theta\cos(n\theta) - \cos\theta\sin(n\theta)\right\} - n\,Dn\left(\frac{L}{2\sin\theta}\right)^{-n-1}\left\{\sin\theta\cos(n\theta) + \cos\theta\sin(n\theta)\right\}\right) = 0$$

$$\text{for } \frac{\pi}{4} \leq \theta \leq \frac{3\pi}{4}$$

$$Co + \sum_{n=1}^{\infty}\left\{Cn\left(-\frac{L}{2\cos\theta}\right)^{n}\cos(n\theta) + Dn\left(-\frac{L}{2\cos\theta}\right)^{-n}\right\}\cos(n\theta) = 0$$

$$\text{for } \frac{3\pi}{4} \leq \theta \leq \pi.$$

The next step in the analysis is to utilize the outer cell edge boundary condition relationships to find the values of the coefficients. The coefficients can be determined using techniques from the calculus of variations. The boundary conditions are rewritten as functions of θ as follows:

$$p^{(n)}(\theta) = Co + \sum_{n=1}^{\infty}\left\{Cnf^{(n)}(\theta) + Dn\,g^{(n)}(\theta)\right\}. \qquad \text{(III-25)}$$

The θ functions are then expanded as Fourier-cosine series

$$f^{(n)}(\theta) = \alpha_o^{(n)} + \sum_{k=1}^{\infty}\alpha_k^{(n)}\cos(k\theta)$$

$$g^{(n)}(\theta) = \gamma_o^{(n)} + \sum_{k=1}^{\infty}\gamma_k^{(n)}\cos(k\theta).$$

To find the coefficients of the θ functions, it is necessary to integrate over all θ in the unit cell. For example, $f(\theta)$ becomes

$$\int_0^{\pi} f^{(n)}(\theta)d\theta = \int_0^{\pi}\left\{\alpha_o^{(n)} + \sum_{k=1}^{\infty}\alpha_k^{(n)}\cos(k\theta)\right\}d\theta. \qquad \text{(III-26)}$$

It was shown earlier, due to orthogonality, that the right-hand side of Equation (III-26) becomes $\alpha_o^{(n)}\pi$. This allows Equation (III-26) to be rewritten as

$$\int_0^{\frac{\pi}{4}} \left(\frac{L}{2\cos\theta}\right)^n \cos(n\theta)d\theta + \int_{\frac{\pi}{4}}^{\frac{3\pi}{4}} n\left(\frac{L}{2\sin\theta}\right)^{n-1} \Big\{\sin\theta\cos(n\theta) - \cos\theta\sin(n\theta)\Big\}d\theta +$$

$$\int_{\frac{3\pi}{4}}^{\pi} \left(\frac{-L}{2\cos\theta}\right)^n \cos(n\theta)d\theta = \alpha_o^{(n)}\pi. \qquad \text{(III-27)}$$

Needing another equation to solve for the unknown α's, the property of orthoganality is again used. Each side of Equation (III-26) was multiplied by $\cos(h\theta)$. Similar to the above expressions, this gave

$$\int_0^{\frac{\pi}{4}} \left(\frac{L}{2\cos\theta}\right)^n \cos(n\theta)\cos(h\theta)d\theta + \int_{\frac{\pi}{4}}^{\frac{3\pi}{4}} n\left(\frac{L}{2\sin\theta}\right)^{n-1} \Big\{\sin\theta\cos(n\theta) - \cos\theta\sin(n\theta)\Big\}$$

$$\cos(h\theta)d\theta + \int_{\frac{3\pi}{4}}^{\pi} \left(\frac{-L}{2\cos\theta}\right)^n \cos(n\theta)\cos(h\theta)d\theta = \frac{\pi}{2}\alpha_{h=k}^{(n)} \qquad \text{(III-28)}$$

An identical procedure was used to set up solutions for $g^{(n)}(\theta)$ in terms of $\gamma_o^{(n)}$ and $\gamma_{h=K}^{(n)}$. Equations (III-27) and (III-28) are converted into a system of linear equations to solve for the α's. Equation (III-27) becomes

$$\begin{bmatrix} \alpha_o^{(1)} \\ \alpha_o^{(2)} \\ \vdots \\ \alpha_o^{(n)} \end{bmatrix} = \frac{1}{\pi} \begin{bmatrix} \left(X_o^{(1)} + Y_o^{(1)} + Z_o^{(1)}\right) \\ \left(X_o^{(2)} + Y_o^{(2)} + Z_o^{(2)}\right) \\ \vdots \\ \left(X_o^{(n)} + Y_o^{(n)} + Z_o^{(n)}\right) \end{bmatrix}$$

where X, Y, and Z are the integrals from Equation (III-27), respectively. Similarly for Equation (III-28),

$$\begin{bmatrix} (\alpha_1^{(1)}) & (\alpha_2^{(1)}) \cdots & (\alpha_h^{(1)}) \\ (\alpha_1^{(2)}) & (\alpha_2^{(2)}) & \vdots \\ \vdots & & \\ (\alpha_1^{(n)}) & & (\alpha_{(h)}^{(n)}) \end{bmatrix} = \frac{2}{\pi} \begin{bmatrix} (X_1^{(1)} + Y_1^{(1)} + Z_1^{(1)}) \cdots (X_h^{(1)} + Y_h^{(1)} + Z_h^{(1)}) \\ \vdots \\ (X_1^{(n)} + Y_1^{(n)} + Z_1^{(n)}) \quad (X_h^{(n)} + Y_h^{(n)} + Z_h^{(n)}) \end{bmatrix}$$

Simpson's numerical integration techniques were used to find the values of the integrals X, Y, and Z. Successive trials were used to determine the number of terms to be carried, (n). For n = odd, the returned value of the sum of the integrals, X + Y + Z, was zero. The value of the sum did not change substantially for n > 10, hence all expansions carried 10 terms. As before, an identical procedure was followed for $\gamma_o^{(n)}$ and $\gamma_h^{(n)}$.

All α's and γ's are now known and Equation (III-25) can be written for each n as

$$P^{(1)}(\theta) = Co + C_1\left(\alpha_o^{(1)} + \sum_{h=1}^{10} \alpha_h^{(1)} \cos(h\theta)\right) + D_1\left(\gamma_o^{(1)} + \sum_{h=1}^{10} \gamma_h^{(1)} \cos(h\theta)\right)$$

$$\vdots$$

$$P^{(10)}(\theta) = Co + C_{10}\left(\alpha_o^{(10)} + \sum_{h=1}^{10} \alpha_h^{(10)} \cos(h\theta)\right) + D_{10}\left(\gamma_o^{(10)} + \sum_{h=1}^{10} \gamma_h^{(10)} \cos(h\theta)\right).$$

The value of $P^{(n)}(\theta)$ changes, depending on the range of θ. This gives rise to a set of linear equations when used in combination with Equations (III-6), (III-8) and (III-13) determines all the constants in the temperature expression. With the constants all known, the temperature at any point in the cell can be found.

Temperatures were calculated at locations that correspond to nodal points in the finite element analysis, and measurement points in the electrical analog. Major matrix manipulation was done using standard International Mathematical and Statistical Libraries, Inc. (IMSL) subroutines.

B. The Finite Element Solution

A computer code was developed by Westinghouse Astronuclear Laboratory (TAP-A) in December, 1969, to solve problems involving transient and steady state heat transfer in multidimensional systems having arbitrary geometric configurations, boundary conditions, initial conditions, heat generation, and physical properties. The program also has the capability to consider such heat transfer modes and boundary conditions as internal conduction and radiation, free and forced convection, radiation at external surfaces, specified time dependent surface temperatures, and specified time dependent surface heat fluxes. Space and time dependent thermal conductivity and heat capacity as well as time dependent external temperatures can be considered.

TAP-A uses explicit or implicit mathematical methods to solve the difference equations. The implicit method uses an overall heat balance on the body being investigated as well as temperature convergence criteria.

To solve for the temperature distribution of an irregular body, the body is divided into a number of small cells. Each cell has associated with it an interior point which is called an interior node. Surfaces of cells which lie on the boundary of the body are associated with one of the surface points and is called a surface node. In this manner a grid or mesh represents the body. Input flexibility allows the grid not to be geometrically uniform. Internal nodes are associated with volumes, heat capacities, and heat generation rates. Surface nodes are associated with areas and film coefficients.

The code ties nodes together with connectors. A connector is a path between two nodes along which heat can flow. Connectors are functions of the material conductivity, and length and areas between nodes. Hence, the code does not recognize any real geometry, only the lengths, areas, and volumes of the nodes and connectors.

The physical characteristics of each node can also be specified allowing for many types of materials. These characteristics include initial temperatures of internal, surface, and boundary nodes, nodal

density (lb/in^3), heat capacity and thermal conductivity of each node, and the film or radiation coefficients for surface to boundary connections. The only drawback to this code is that it uses English units, and would require tremendous effort to convert to a more usable form. Table I summarizes these conditions for the unit cell.

The unit cell can be modeled as shown in Figure 5. By using TAP-A on the unit cell, an effective conductivity can be found that can be used to further assess the two-dimensional effective conductivity found from the analytical solution.

To increase or decrease the porosity of the cell, it is only necessary to add or subtract rows of nodes from the outside edge of the standard case shown in Figure 5. In this manner, the internal nodal structure along the material interface, which has a complex geometry, need only be calculated once.

The 19.6% porosity case was chosen to be the base case, and the unit cell normalized to a length of 1.0. Removing one row along each outside edge produced a length of 0.875 and a porosity of 25.65%. In a similar manner, other porosities are created. Table II summarizes the porosities, and sizes of the various cells.

The resulting nodal patterns for 8.4%, 12.6%, 19.6%, 25.6%, 34.9%, and 50.3% porosity are shown in Appendix D with the accompanying temperature distribution through the cell. It is immediately apparent that each cell is symmetric about the horizontal axis which is an expected result since there are no sources or sinks in the unit cell.

TABLE I. INITIAL PHYSICAL CHARACTERISTICS OF THE UNIT CELL.

Characteristic	Metric Units	English Units
Top Boundary Temperature	1°C	493.8°R
Bottom Boundary Temperature	0°C	492.0°R
Initial Internal Nodal Temperatures	0.4°C	492.7°R
Ceramic Material Density	10.79 g/cm^3	0.39 lb/in^3
Pore Material Density	0.0182 g/cm^3	6.53×10^{-4} lb/in^3
Ceramic Material Heat Capacity	251.98 cal/g-°C	1.0 BTU/lb-°R
Pore Material Heat Capacity	251.98 cal/g-°C	1.0 BTU/lb-°R
Ceramic Material Thermal Conductivity	0.023 w/cm-°C	3.08×10^{-5} BTU/sec in °R
Pore Material Thermal Conductivity	0.00018 w/cm-°C	2.46×10^{-7} BTU/sec in °R
Top Surface Film Coefficient	2.943×10^6 w/cm^2-°C	10000. $BTU/sec\text{-}in^2$-°R
Bottom Surface Film Coefficient	2.943×10^6 w/cm^2-°C	10000. $BTU/sec\text{-}in^2$-°R

TABLE II. UNIT CELL SIZE AND POROSITY SUMMARY.

Case Number	Porosity	Cell Length	Cell Width
1	8.4%	1.500	0.7500
2	12.6%	1.250	0.6250
3	19.6%	1.000	0.5000
4	25.6%	0.875	0.4375
5	34.9%	0.750	0.3750
6	50.3%	0.625	0.3125

FIGURE 5.
NODAL ARRANGEMENT FOR TAP-A UNIT CELL ANALYSIS

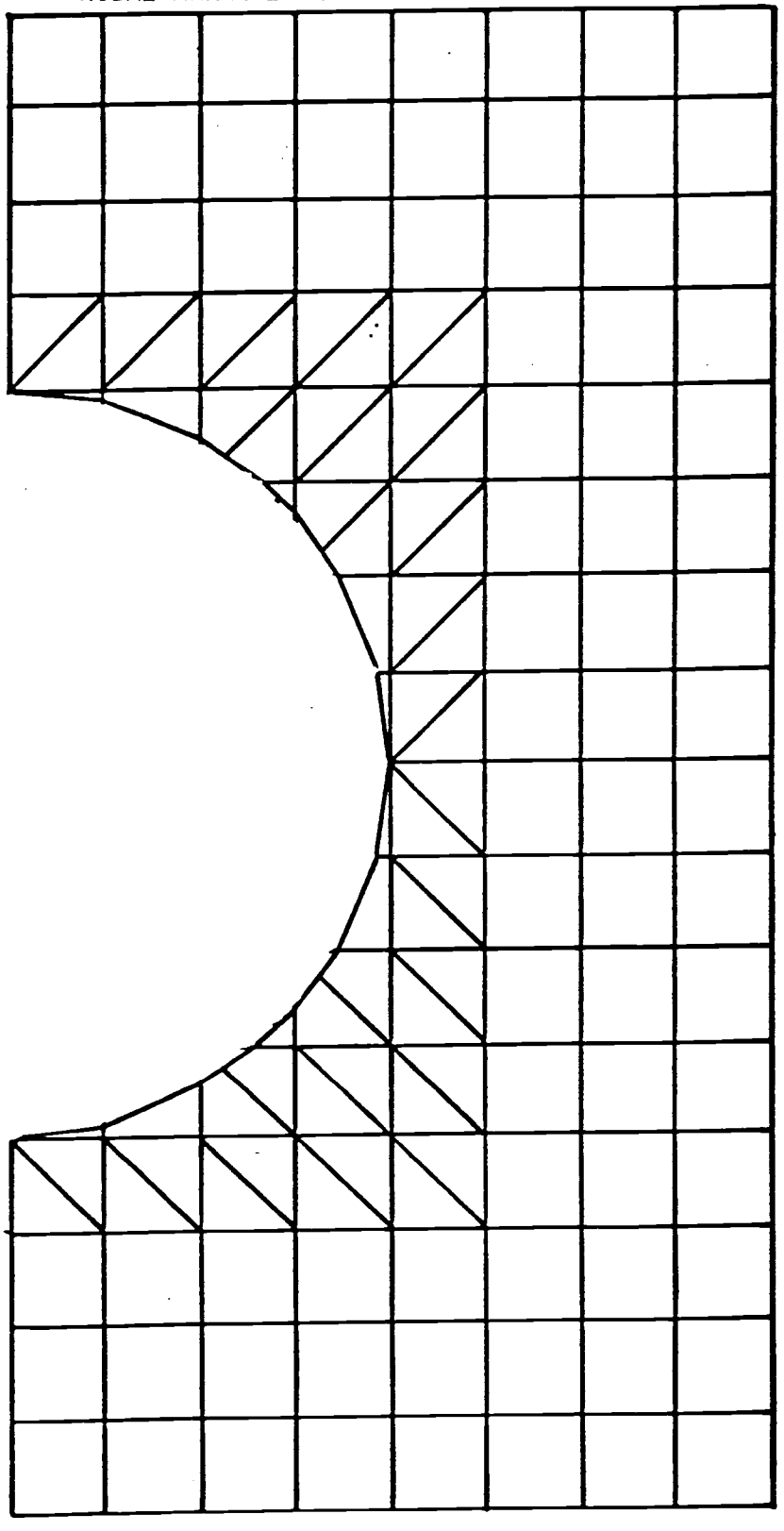

C. The Electrical Analog Solution

The direct mathematical similarity between heat and electrical conduction is well known and used frequently in the study of complex heat conduction problems. The analogy can be immediately recognized when comparing the governing partial differential equations for electrical potential, e, with the partial differential equation for temperature, T:

$$\frac{\partial^2 e}{\partial x^2} + \frac{\partial^2 e}{\partial y^2} = R_L C_L \frac{\partial e}{\partial t}$$

and

$$\frac{\partial^2 T}{\partial x^2} + \frac{\partial^2 T}{\partial y^2} = \frac{1}{\alpha} \frac{\partial T}{\partial t} .$$

These equations are valid for two-dimensional regions with uniform electrical resistance per unit length, R_L, uniform electrical capacity per unit length, C_L, and uniform thermal diffusivity, α. The transient analogy is complete if on the same time scale, dt, the electrical diffusivity, $\frac{1}{R_L C_L}$, and the thermal diffusivity, α, are equal. Two laws are then true for the system; the conservation of charge in the electrical system corresponds to the conservation of heat in the thermal system, and current flow obeying Ohm's Law corresponds to heat flow obeying Fourier's Law.

The steady state analogy used in this paper is completed by the conditions $\frac{\partial e}{\partial t} = 0$, and $\frac{\partial T}{\partial t} = 0$, and noticing that both equations now satisfy the simple Laplace equation for steady state conditions with no internal sinks or sources. Therefore, a steady electric potential field e(x,y) can be regarded as the analog of a steady temperature field T(x,y). Equipotential lines in the voltage field correspond to isotherms in the temperature field. Table III sums up the analogy.

TABLE III. SUMMARY OF ELECTRICAL AND THERMAL ANALOGY.

Electrical		Thermal	
Charge	$= Q_e$ (coulomb)	Heat	$= Q$ (BTU)
Voltage	$= e$ (volts)	Temperature	$= T$ (°F)
Resistance	$= R$ (ohms)	Resistance	$= R \frac{hr - °F}{BTU}$
Current	$= i$ (amps) $= \frac{\Delta e}{R}$	Flow	$= q \frac{BTU}{hr} = \frac{\Delta T}{R}$

There are several types of electrical modes used to simulate the temperature field. One method is the electrolytic bath where an electrolyte of constant resistivity is contained in a shallow basin similar in shape to the actual problem. The boundaries of the basin are constructed of electrical conducting material or insulator to simulate boundary conditions. This method requires rather elaborate and laborious setup methods and recording techniques, although it produces satisfactory accuracy.

An easier method is the use of teledeltoes electrical conduction paper. This paper has uniform resistance characteristics and is used in place of the electrolytic bath. Teledeltoes paper has the advantage of being a permanent medium on which to work, and the plots are easy to prepare and record. The paper is cut to the desired shape, placed on a flat, nonconducting surface, and a voltage difference is introduced by attaching low resistance, metallic electrodes to the surface. Boundary conditions are simulated by cutout "blank" areas in the paper, or by applying resistance wire elements, bare copper wires, or conducting areas of silver paint to the surface of the paper as each problem dictates. A voltage divider is used to select a desired percentage of the applied potential which is compared to the potential at any given point on the paper through a microammeter. For direct comparison to the finite element method, the nodal points were chosen. A null indication shows that the potentials are equal.

The sample setup is shown in Figure 6. The top and bottom edges of the unit cell are silver painted to provide uniform voltage along these edges which correspond to fixed temperatures. At the top, the temperature equals one, and along the bottom edge, the temperature equals zero. For ideal results, the sheet would be infinite in size. This is impractical, and the sheets used were approximately 30 centimeters by 15 centimeters. The pore area was cut out of the sheet to simulate a no heat transfer condition across the pores. Readings were taken at locations which correspond to the nodel points of the finite element solution. The field plotter readings showed little or no sensitivity to pressure, but other sources of error are possible. These include nonuniformity of the conducting paper, circuit nonlinearity, and the ability to locate exactly the nodal point.

FIGURE 6.
ANALOG FIELD PLOTTER SAMPLE SET UP

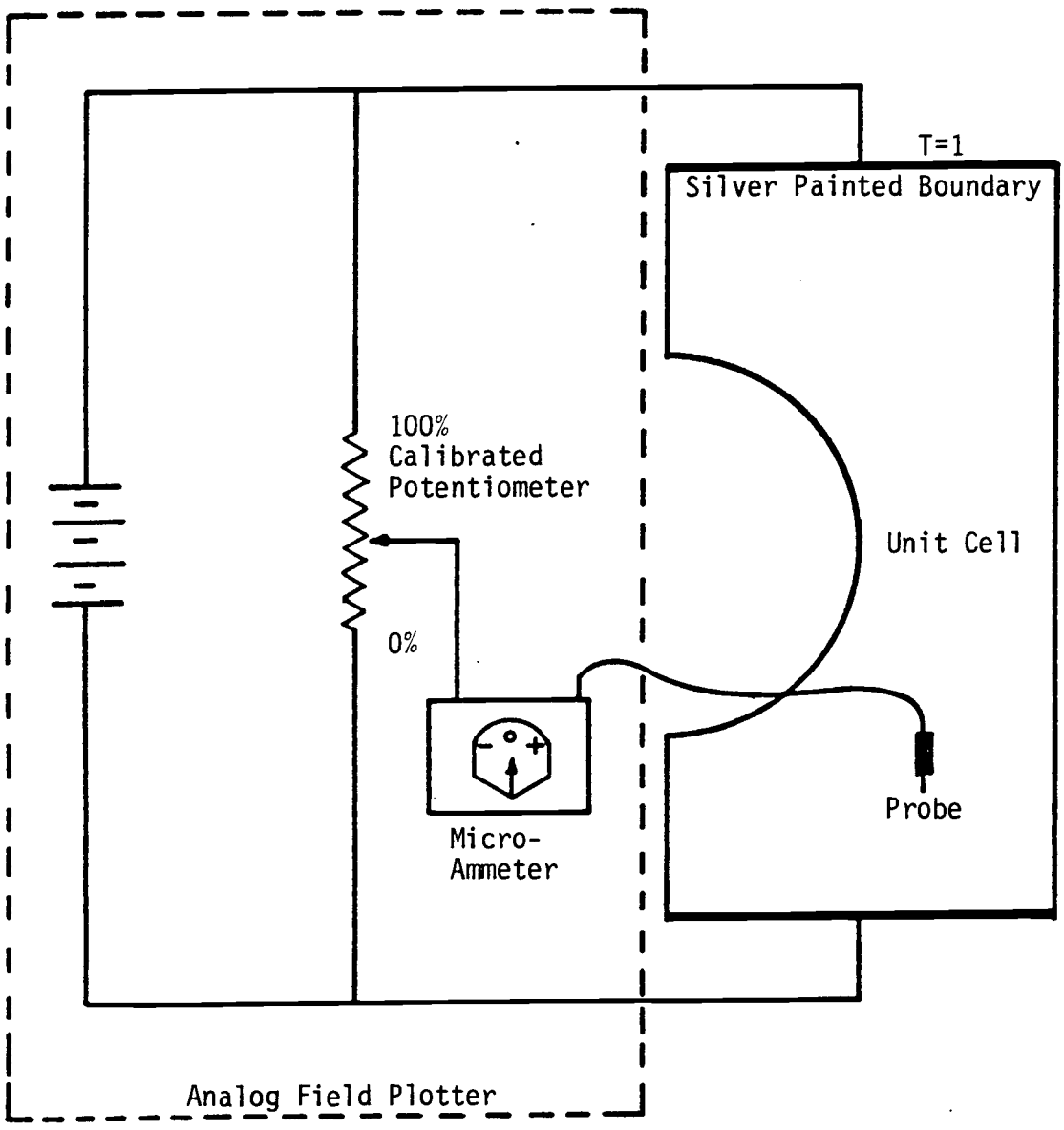

IV. EFFECTIVE CONDUCTIVITY CALCULATION

Once the temperature field throughout the unit cell is found, calculation of the effective conductivity can be performed. Recalling the definition of heat flux as

$$q = - K \frac{dT}{dX} \qquad \text{(IV-1)}$$

it is possible to determine the effective conductivity. Integration of both sides of the above expression with respect to the surface area through which the heat flows yields

$$\int_A q dA = \int_A - K \frac{dT}{dX} dA. \qquad \text{(IV-2)}$$

Breaking the resulting expression into a summation over all nodal points, j, along the boundary gives

$$\sum_j q_j A_j = \sum_j - K \frac{dT}{dX}\Big|_j A_j . \qquad \text{(IV-3)}$$

Using the approximations

$$q = \frac{\sum_j q_j A_j}{\sum_J A_j}$$

and

$$\frac{dT}{dX}\Big|_j = \frac{T_{top} - T_{1,j}}{\Delta X_j}$$

gives final expression for the heat flux

$$q = \frac{-K \sum_j \frac{T_{top} - T_{1,j}}{\Delta x_j}}{\sum A_j} A_j \qquad \text{(IV-4)}$$

The conductivity, K, in this expression is a known quantity, and corresponds to the 100% dense material, or other reference density. Since the unit cell contains no sources or sinks, the heat flow in through the top must equal the heat flow out through the bottom. Having determined q and knowing the temperatures at the top and bottom of the cell, the following expression is developed

$$q = -K_p\left(\frac{T_{top} - T_{bottom}}{L}\right)$$

where K_p = the effective conductivity of the porous cell
L = the length of the unit cell
q = the heat flux through the unit cell.

All quantities in this expression are known except K_p.

A sample calculation will be helpful. For the 8.38% porosity case, the situation in Figure 7 was observed for the first row of nodes from TAP-A. Solution for the entire surface is shown in Appendix D. For each porosity case, an assumed conductivity value of the 100% dense material was 0.023 w/cm-°C. This value is not particularly important since a ratio of the true value to the effective value is the goal of the paper. The solution for the heat flux, q, becomes

$$q = \frac{0.023\left\{\frac{3(1 - 0.97)\ 0.125}{0.0625} + \frac{3(1 - 0.96)\ 0.125}{0.0625}\right\}}{0.75} = 0.0129.$$

Referring to Figure 7, each node for this case is 0.125 units wide representing the nodal surface area through which heat flows, and the distance from the top edge where T=1, to the nodal point is 0.0625.

Substituting into the expression for K_p yields

$$0.0129 = -K_p \left\{ \frac{1 - 0}{1.5} \right\}$$

or $K_p = 0.01932$ (w/cm-°C). A summary of the effective conductivities found from TAP-A is shown in Table IV.

TABLE IV. SUMMARY OF EFFECTIVE CONDUCTIVITY WITH CHANGING POROSITY (TAP-A).

Porosity (%)	q	K_p (w/cm-°C)	K_p/K
8.38	0.01288	0.01932	0.84
12.57	0.01398	0.01748	0.76
19.63	0.01472	0.01472	0.64
25.65	0.01472	0.01288	0.56
34.91	0.01349	0.01012	0.44
50.27	0.01104	0.00690	0.30

For comparison, the same information from the electrical analog solution is shown in Table V. This information was taken from an interior node to minimize boundary effects due to the silver paint.

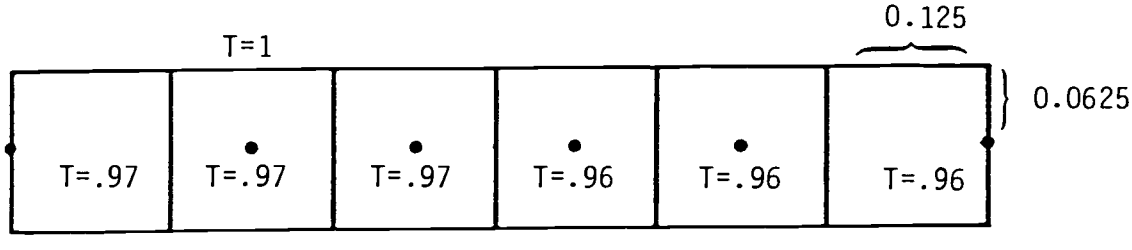

Figure 7. Temperature Distribution for the First Nodal Row from TAP-A, 8.37% Porosity Case.

TABLE V. SUMMARY OF EFFECTIVE CONDUCTIVITY WITH CHANGING POROSITY (ELECTRICAL ANALOG)

Porosity (%)	q	K_p (w/cm-°C)	K_p/K
8.38	0.01263	0.01895	0.824
12.57	0.01384	0.01730	0.752
19.63	0.01444	0.01444	0.628
25.65	0.01430	0.01251	0.544
34.91	0.01312	0.00984	0.427
50.27	0.01067	0.00667	0.290

Table 6 shows the information for the two-dimensional analytical solution described in Section III.

TABLE VI. SUMMARY OF EFFECTIVE CONDUCTIVITY WITH CHANGING POROSITY (2-D ANALYTICAL SOLUTION)

Porosity (%)	q	K_p (w/cm-°C)	K_p/K
8.38	0.01283	0.01925	0.837
12.57	0.01393	0.01741	0.757
19.63	0.01461	0.01461	0.635
25.65	0.01451	0.01270	0.552
34.91	0.01331	0.00998	0.434
50.27	0.01086	0.00679	0.295

V. POROSITY CORRECTION RELATIONSHIPS

To make the data in Tables IV through V more useful in predicting thermal conductivities of ceramic nuclear fuels of known porosity, a series of curves were fit. First to be fit were quadratic equations of the form

$$\frac{K_p}{K} = A + Bp + Cp^2. \qquad \text{(V-1)}$$

This was done using standard least-squares fitting as shown in Figure 8.

Figure 8. Quadratic Fit to the Data Using Least Squares Technique.

$$\begin{bmatrix} N & \sum_i p_i & \sum_i p_i^2 \\ \sum_i p_i & \sum_i p_i^2 & \sum_i p_i^3 \\ \sum_i p_i^2 & \sum_i p_i^3 & \sum_i p_i^4 \end{bmatrix} \begin{bmatrix} A \\ B \\ C \end{bmatrix} = \begin{bmatrix} \sum_i \left(\frac{K_p}{K}\right)_i \\ \sum_i p_i \left(\frac{K_p}{K}\right)_i \\ \sum_i p_i^2 \left(\frac{K_p}{K}\right)_i \end{bmatrix}$$

where N = number of data points

A,B,C = coefficients of the quadratic equation

and

$$\frac{K_p}{K} = A + Bp + Cp^2$$

Using a 3 x 3 matrix solver in the Hewlett-Packard 67 to solve the system, an expression for (K_p/K) in terms of porosity, p, was found for the finite element data to be

$$\frac{K_p}{K} = 1.0048 - 2.1134\ p + 1.4166\ p^2; \qquad \text{(V-2)}$$

for the electrical analog data

$$\frac{K_p}{K} = 0.9939 - 2.1335\ p + 1.4589\ p^2; \qquad \text{(V-3)}$$

and for the analytical solution

$$\frac{K_p}{K} = 1.0164 - 2.2599\ p + 1.65972\ p^2. \qquad \text{(V-4)}$$

To illustrate their use, the 8.38% porosity case would be solved for the electrical analog as follows:

$$\frac{K_p}{K} = 0.9939 - 2.1335\ (.0838) + 1.4589\ (.0838)^2 = 0.8254.$$

Table VII summarizes the comparison of these expressions for the remaining porosities. As can be seen, there is little difference between them as expected.

TABLE VII. COMPARISON OF CASE DATA TO QUADRATIC FITS

Porosity	TAP-A	TAP-A Quadratic	Electrical Analog	Electrical Quadratic	Analytical	Analytical Quadratic
0.0838	0.840	0.838	0.824	0.825	0.837	.839
0.1257	0.760	0.762	0.752	0.749	0.757	.759
0.1963	0.640	0.645	0.628	0.631	0.635	.637
0.2565	0.560	0.556	0..544	0.543	0.552	.546
0.3491	0.440	0.440	0.427	0.427	0.434	.430
0.5027	0.300	0.300	0.290	0.290	0.295	.300

The data was also compared to empirical formulas used in previous studies, and expressions of similar form were found. In particular, it is compared to the formula found by Cunningham[6]

$$\frac{K_p}{K} = e^{-2.14p}$$

and to an expression found by one-dimensional heat flow analysis (no heat flow is allowed around the pore) as shown in Appendix C:

$$\frac{K_p}{K} = 1 - \frac{2}{\pi^{1/2}} p^{1/2}$$

To fit expressions of similar form to the actual data the least squares technique was applied to a transformation of the equations. To fit a Cunningham-type expression of

$$\frac{K_p}{K} = e^{ap}$$

it was necessary to transform the equation to

$$\ln \frac{K_p}{K} = ap.$$

The least squares parameter, γ, is defined as

$$\gamma = \sum_i \left(\ln \left(\frac{K_p}{K} \right)_i - aPi \right)^2$$

Minimizing γ is the principle of least squares fitting and is accomplished by taking the partial derivative of γ with respect to a, and setting the resulting expression to zero. This gave

$$\frac{\partial \gamma}{\partial a} = \sum_i \left(-2P_i \ln \left(\frac{K_p}{K} \right)_i - 2aP^2 i \right) = 0.$$

Simplifying this expression leaves

$$a = \frac{\sum_i \ln \left(\frac{K_p}{K} \right)_i}{\sum_i Pi} .$$

Using the finite element data yielded a value of

$$a = -2.31$$

or

$$\frac{K_p}{K} = e^{-2.31P}$$

where P is porosity as a fractional amount, i.e., .0838 for 8.38%.

Using the same technique, an expression was found for the one-dimensional heat flow case of the form for the finite element data

$$\frac{K_p}{K} = 1 + bP^{1/2}.$$

The value of b was found to be

$$b = -0.850$$

hence

$$\frac{K_p}{K} = 1 - 0.85P^{1/2}$$

where P is also a fractional amount. Table VIII compares these expressions with those of Cunningham and the one-dimensional heat flow case for each porosity value. Tables IX and X do likewise for the electrical analog and analytical solutions.

Close examination of Tables VIII, IX, and X is warranted. It is readily apparent that the one-dimensional heat flow solutions are inadequate predictors of the effective conductivity ratio and should not be considered as an accurate porosity correction formula. The data fitted curves yield reasonable results for both quadratics (Table VII) and exponential forms. The important column is the solution of Cunningham and how well it agrees with the finite element solution of TAP-A, the electrical analog solution, and the two-dimensional analytical solution. The Cunningham solution predicts values of effective conductivity, $\frac{K_p}{K}$, which are consistently within a few percent of the experimental data. This close agreement tends to lend support to the three-dimensional solution method of Cunningham. Table XI summarizes this result.

TABLE VIII. COMPARISON OF VARIOUS CURVE FITS TO FINITE ELEMENT DATA FOR $\left(\frac{K_p}{K}\right)$.

Porosity	TAP-A	Cunningham Solution*	-2.31P e**	$1 - \frac{2}{\pi} P^{1/2}$***	$1 - 0.85 P^{1/2}$****
0.0838	0.840	0.836	0.824	0.673	0.754
0.1257	0.760	0.764	0.748	0.600	0.699
0.1963	0.640	0.657	0.635	0.500	0.623
0.2565	0.560	0.577	0.553	0.429	0.569
0.3491	0.440	0.459	0.446	0.333	0.498
0.5027	0.300	0.250	0.313	0.200	0.397

* Cunningham solution (see Page 3 for porosity ranges)

** TAP-A data solution

*** Theoretical one-dimensional solution

**** TAP-A data solution in one-dimensional form

TABLE IX. COMPARISON OF VARIOUS CURVE FITS TO ELECTRICAL ANALOG DATA FOR $\left(\frac{K_p}{K}\right)$.

Porosity	Electrical Analog	Cunningham Solution*	-2.405P e**
0.0838	0.824	0.836	0.817
0.1257	0.752	0.764	0.739
0.1963	0.628	0.657	0.624
0.2565	0.544	0.577	0.540
0.3461	0.427	0.459	0.432
0.5027	0.290	0.250	0.298

* Cunningham solution (see Page 3 for porosity ranges)

** Electrical analog data solution

TABLE X. COMPARISON OF VARIOUS CURVE FITS TO ANALYTICAL SOLUTION DATA FOR $\left(\frac{K_p}{K}\right)$.

Porosity	Analytical Solution	Cunningham Solution*	$-2.35P_e$**
0.0838	0.837	0.836	0.821
0.1257	0.757	0.764	0.744
0.1963	0.635	0.657	0.630
0.2565	0.552	0.577	0.547
0.3491	0.434	0.459	0.440
0.5027	0.295	0.250	0.307

* Cunningham solution (see Page 3 for porosity ranges)

** Analytical data solution

TABLE XI. COMPARISON OF CUNNINGHAM SOLUTION TO EXPERIMENTAL METHODS FOR EFFECTIVE CONDUCTIVITY $\left(\frac{K_p}{K}\right)$.

Porosity	Cunningham Solution*	Two-Dimensional Analytical Solution	Finite Element TAP-A Solution	Electrical Analog Solution
0.0838	0.836	0.837	0.840	0.824
0.1257	0.764	0.757	0.760	0.752
0.1963	0.657	0.635	0.640	0.628
0.2565	0.577	0.552	0.560	0.544
0.3491	0.459	0.434	0.440	0.427
0.5027	0.250	0.295	0.300	0.290

* Cunningham solution (see Page 3 for porosity ranges)

VI. RANDOM PORE ARRANGEMENT

Pores in ceramic nuclear fuels tend to assume disklike shapes which resemble the lentil plant, and are hence called lenticular pores.[7] These pores migrate toward the hot center of the fuel pellet. As more and more of these pores cluster about the center of a fuel pellet, a central void is formed.

This situation was approximated by distributing pores throughout the unit cell with normal random distributions of (0,1) and (0,2). Figures 9 and 10 show samples of pore locations. The (x,y) coordinates of the pore were determined by the random number generator. Only two pores were allowed in each square of the grid. As can be seen, a tendency to form a central void is simulated.

To find the effective conductivity of these unit cells, the electrical analog technique was used. The conducting paper was cut to approximate the pore locations. This is shown in Figure 11. As was done previously, boundary conditions were set up to induce heat flow from the top to bottom of the cell, i.e., T = 1.0 on the top, and T = 0.0 at the bottom. The temperature profile was then found along a row of nodal points. From this data, the heat flux and effective conductivity were found. Table XII summarizes the results of both cases.

A series of porosities based on a (0,2) distribution was not pursued after the case shown in Figure 10 yielded nearly identical results for the effective conductivity as did the (0,1) distribution shown in Figure 9 and Table XII.

Both the Cunningham and two-dimensional solutions give a good approximation to the results found by the electrical analog experimental procedure. The Cunningham solution gave results that were within just a few percent of the electrical analog for all cases except when porosity was 50%. The two-dimensional solution was consistently within a few percent. These results again lend support to the Cunningham solution as a porosity correction formula.

TABLE XII. COMPARISON OF EFFECTIVE CONDUCTIVITY FOR RANDOM PORE ARRANGEMENT WITH (0,1) DISTRIBUTION TO OTHER CORRECTION FORMULAS

Porosity	Electrical Random Pore	Cunningham Solution*	$e^{-2.35P}$**	Electrical Analog Quadratic***
.094	0.820	0.818	0.802	.806
.125	0.767	0.765	0.745	.750
.199	0.639	0.653	0.626	.627
.223	0.608	0.621	0.592	.591
.344	0.459	0.459	0.446	.433
.500	0.317	0.250	0.309	.292

* Cunningham solution (see Page 3 for porosity ranges)

** Two-dimensional analytical solution

*** $\frac{K_p}{K} = 0.9939 - 2.1335P + 1.4589\ P^2$

FIGURE 9.
RANDOM PORE ARRANGEMENT FOR (0,1) GENERATOR -
22.3% POROSITY

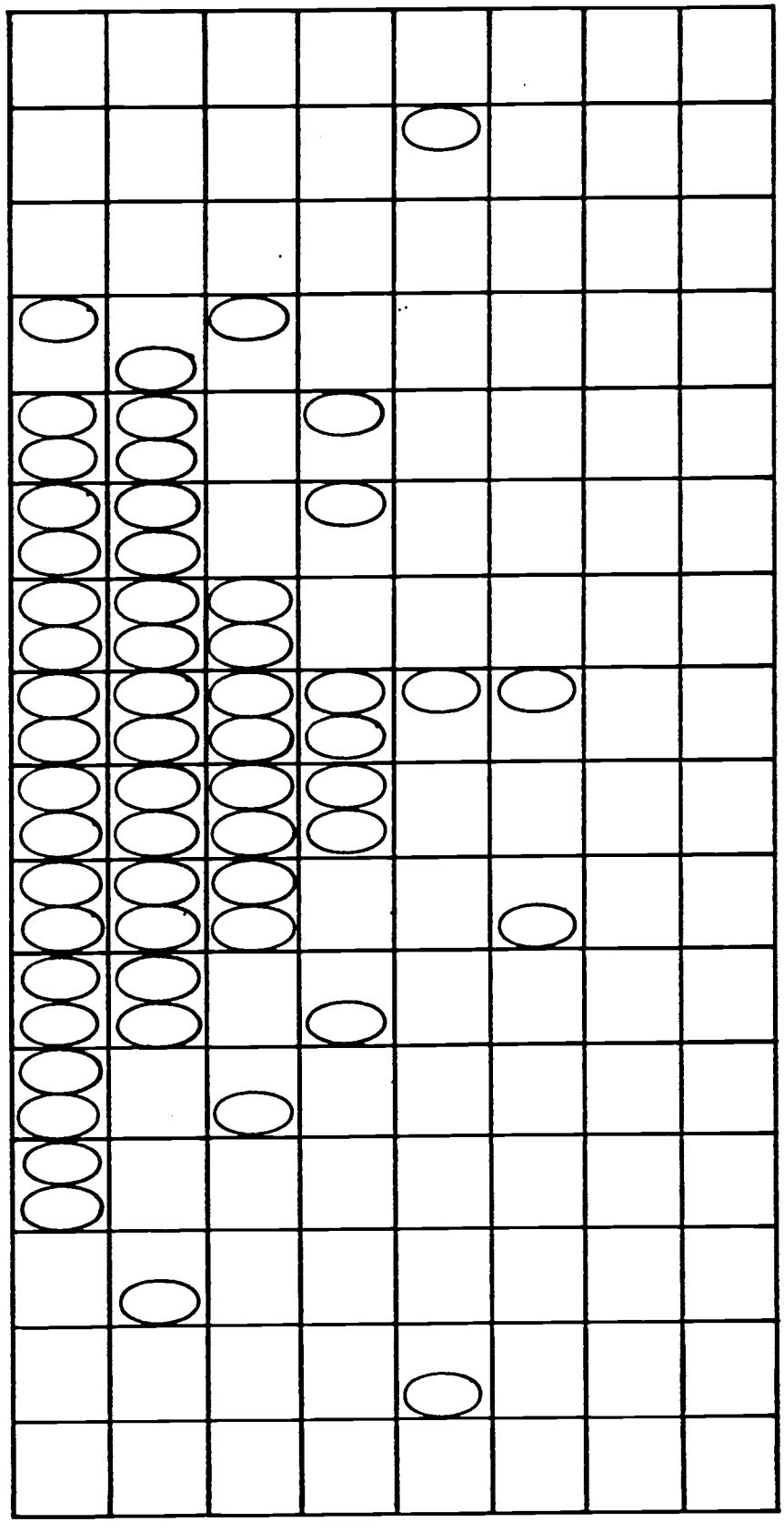

FIGURE 10.
RANDOM PORE ARRANGEMENT FOR (0,2) GENERATOR -
19.9% POROSITY

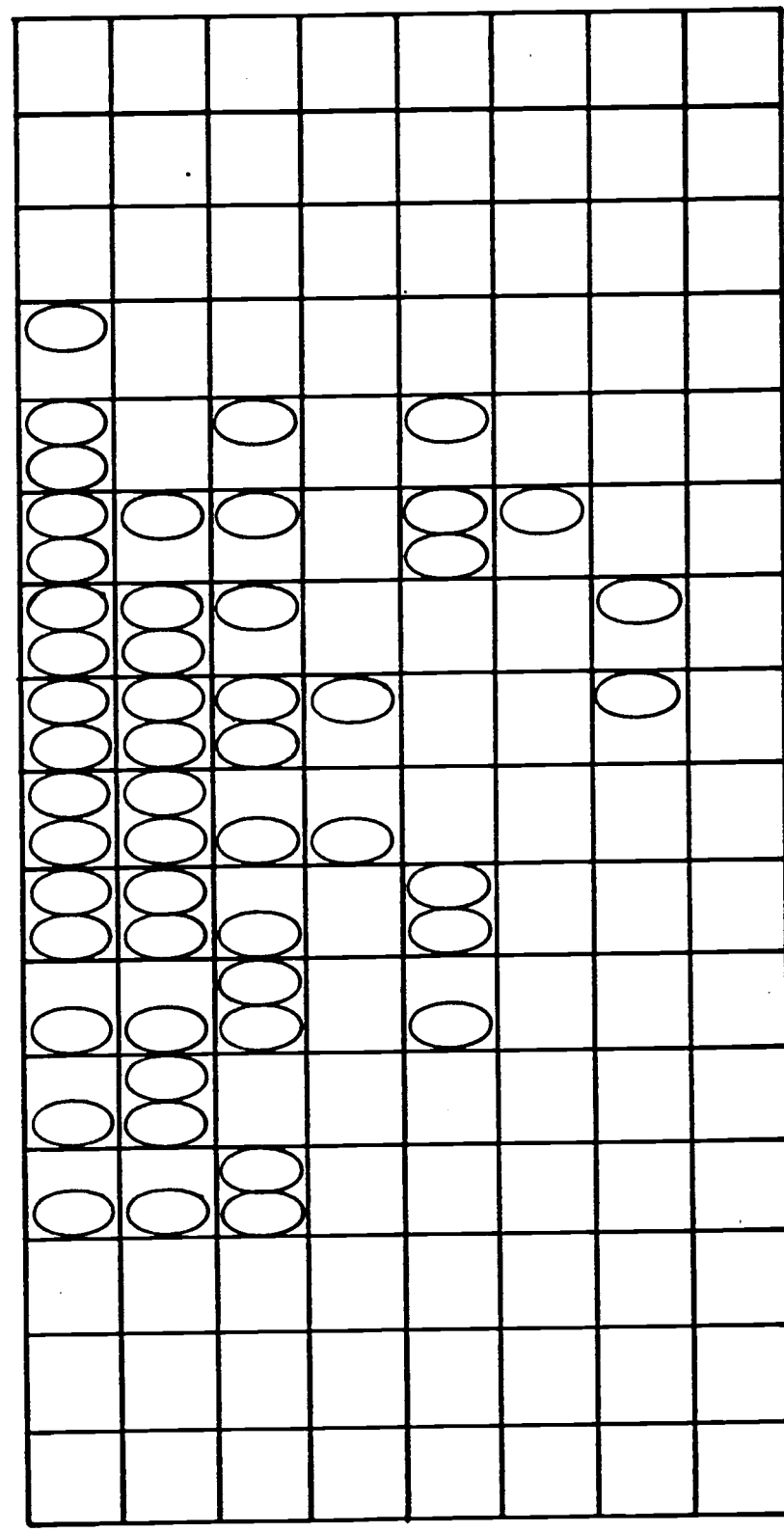

FIGURE 11.
ELECTRICAL ANALOG APPROXIMATION OF (0,1)
RANDOM PORE ARRANGEMENT - 22.3% POROSITY

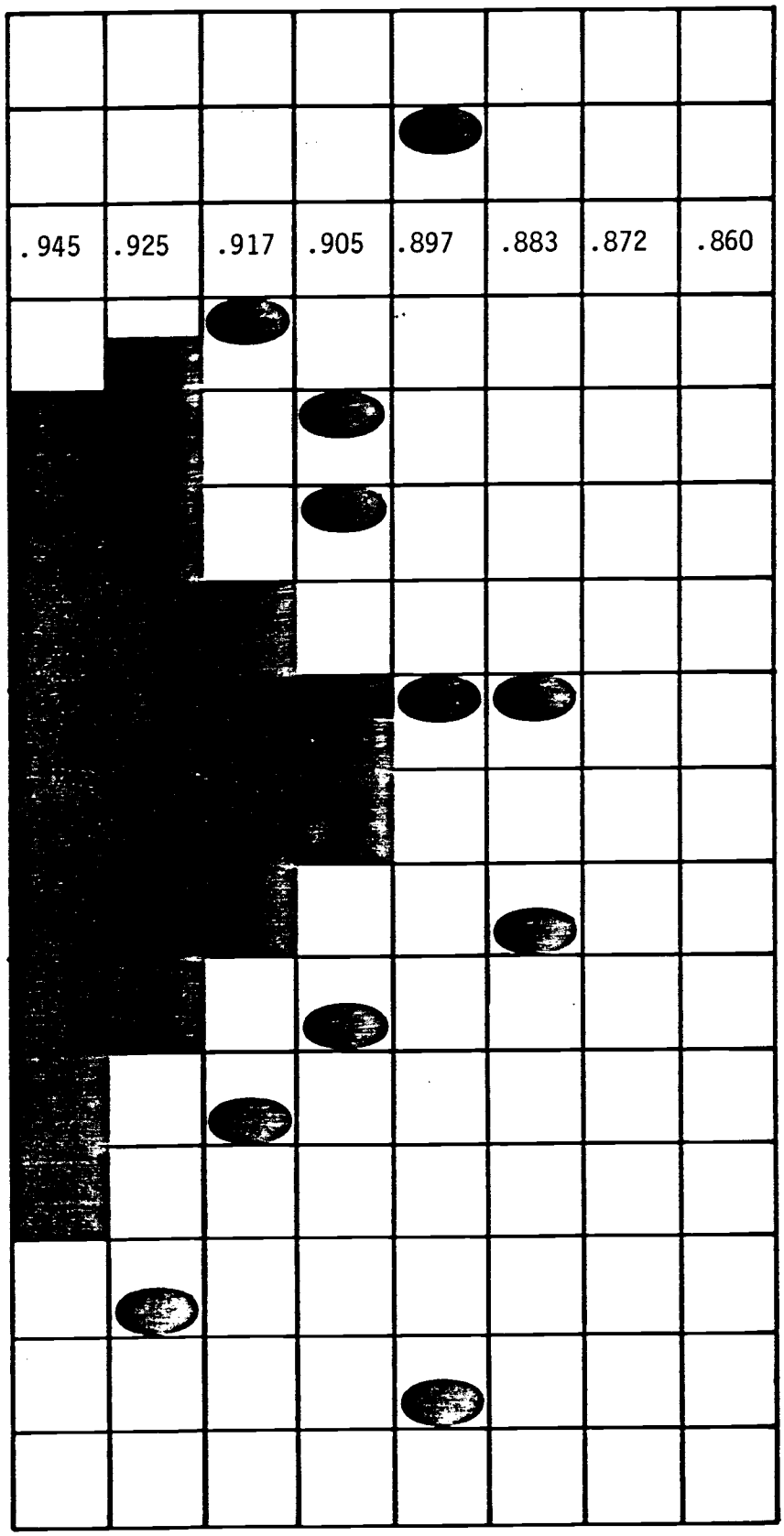

VII. SUMMARY AND CONCLUSIONS

The characteristic heat transfer in ceramic nuclear fuels is an important factor in the design and operation of reactor cores. The heat transfer characteristics are complicated by the presence of entrained porosity. Porosity comes about due to fabrication effects, fission gas formation, and pellet cracking. A porosity correction factor is typically defined which modifies the thermal conductivity of either the 100% dense solid, or some other reference density to account for the presence of the porosity in heat transfer calculations.

Several approaches have been taken to determine this factor. These include empirical methods resulting from experimentation, and analytical methods. The initial analytical methods allowed for heat flow in one direction only with no heat flow around the pore. The next step in analytical solutions was to allow for multidimensional heat flow, and Cunningham produced a three-dimensional solution by solving the heat conduction equations. The heat flux entering and leaving the unit cell was determined, and an effective conductivity found. This effective conductivity was then compared to the conductivity of 100% dense material generating a ratio dependent on porosity, and used as a correction formula.

The purpose of this work was to assess the method of Cunningham by performing a two-dimensional analytical study which was then compared to idealized measurements using an electrical analog for heat flow. An effective conductivity determined as a ratio produced a conductivity correction formula as a function of porosity. For direct comparison, measurements were made using resistance paper, determining the value of the temperature at any point in the system. A finite element code modeling the unit cell was also used to provide the value of the temperature at certain nodal points throughout the system. The electrical analog and the finite element code were used to assess the solutions found by the analytical approach.

All three two-dimensional methods gave results which support the Cunningham methodology. Figure 12 shows a comparison of the analytical

solutions to the results obtained from the electrical analog. The two-dimensional analysis and that of Cunningham consistently lie within a few percent of the electrical analog. Further confidence was gained when predictions from other methodologies were compared to the electrical analog. An illustration of this is shown in Figure 13 where a comparison is shown between Cunningham, the electrical analog, and a solution which allowed only one-directional heat flow. As was shown earlier, the Cunningham and electrical analog solutions have good agreement, while the one-dimensional solution yields completely inadequate results.

As a point of interest, a less-than-ideal unit cell was modeled with the electrical analog and compared to analytical predictions. This was done by distributing large pores in a normal random fashion centered at the middle of the unit cell. A temperature profile was determined and an effective conductivity found. Figure 14 shows these results compared to Cunningham and the two-dimensional analysis. As was the case in Figure 12, there is little to choose from when comparing the methods. All the methods show fine agreement up to porosities of 40%. There is some divergence from experimental results at that point. The methodology of Cunningham is a valid approach to the problem of predicting effective conductivities.

FIGURE 12

COMPARISON OF ANALYTICAL SOLUTIONS TO ELECTRICAL ANALOG

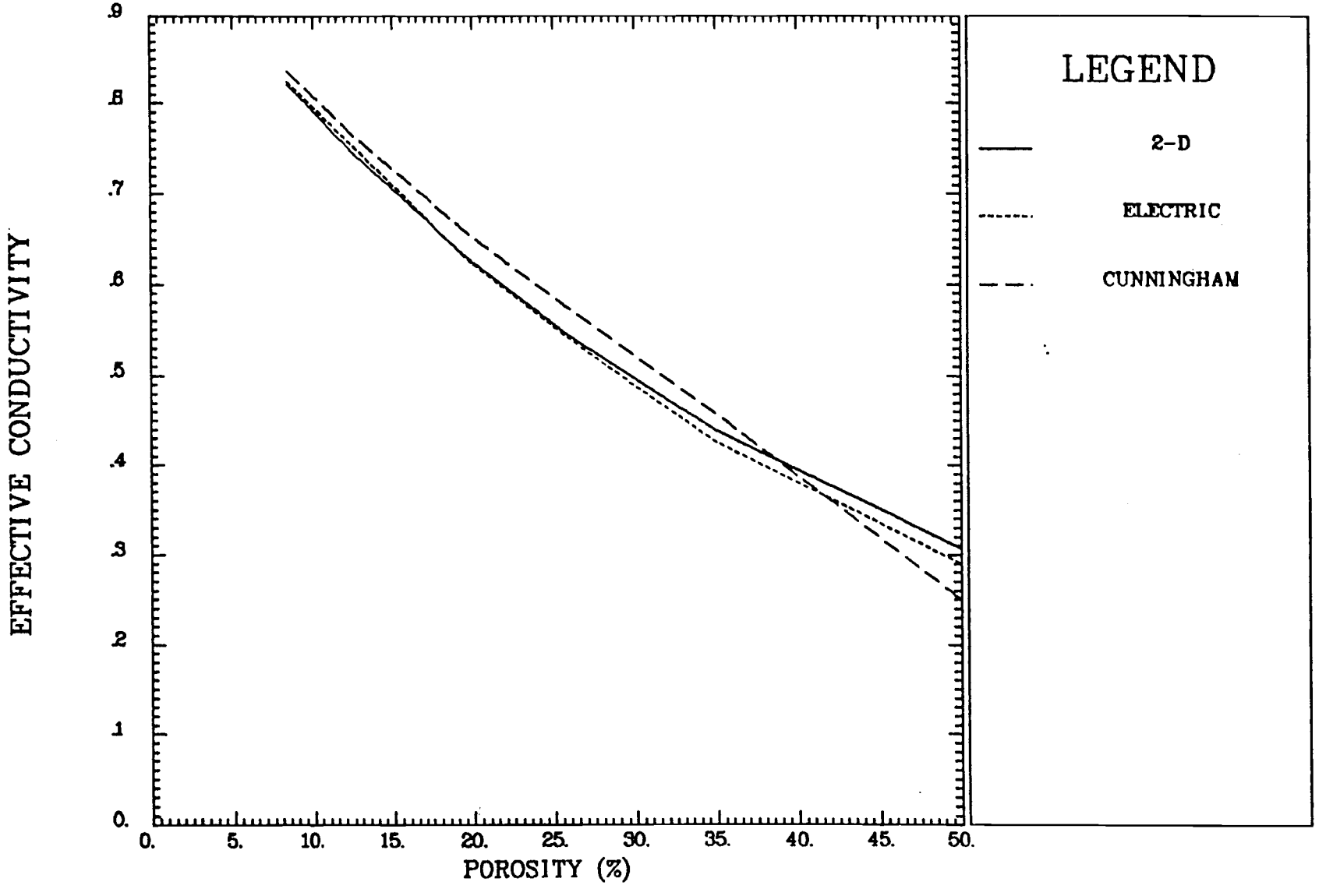

FIGURE 13

COMPARISON OF ONE-DIMENSIONAL SOLUTION TO ELECTRICAL ANALOG

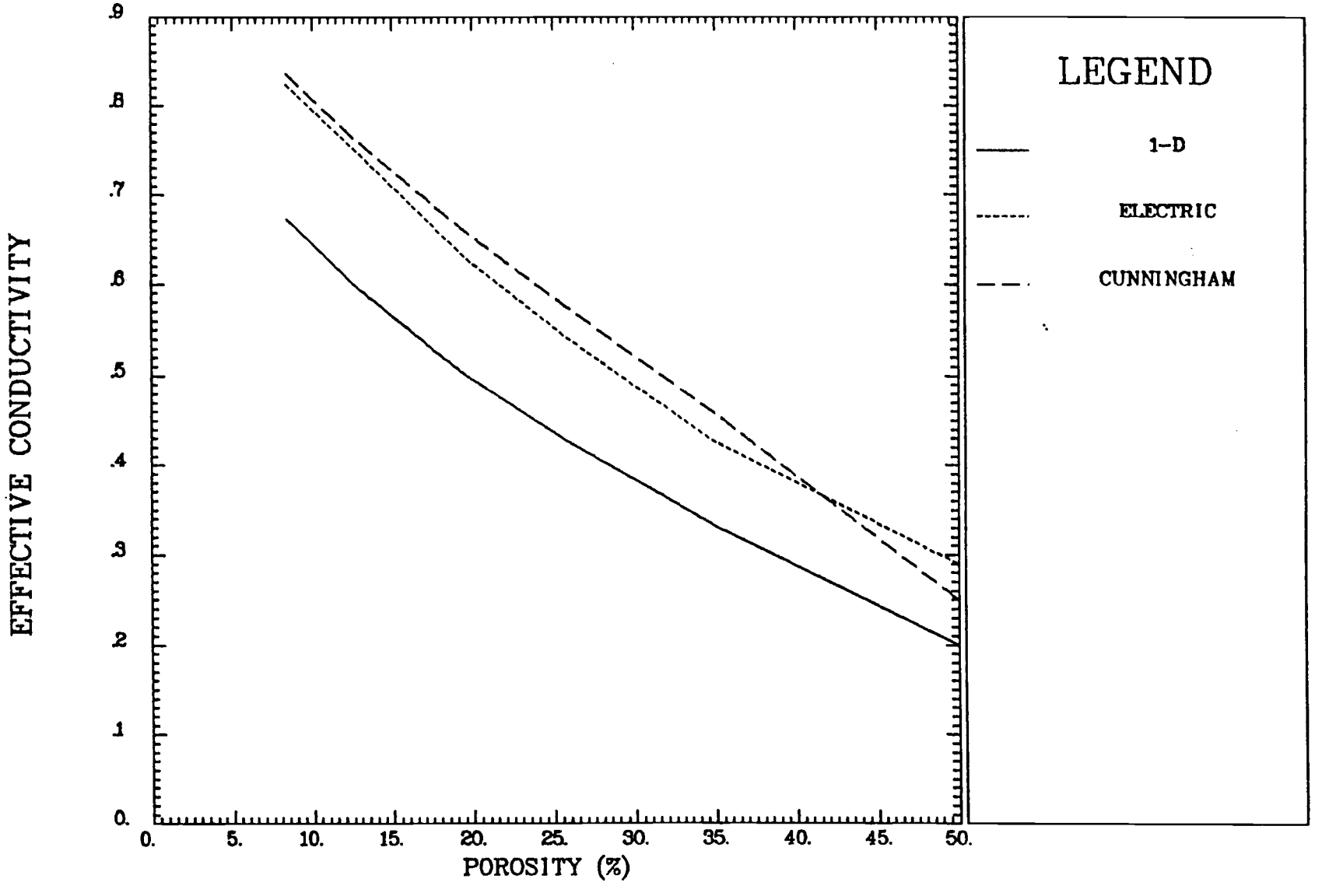

FIGURE 14

COMPARISON OF ANALYTICAL SOLUTIONS TO RANDOM PORE ANALOG

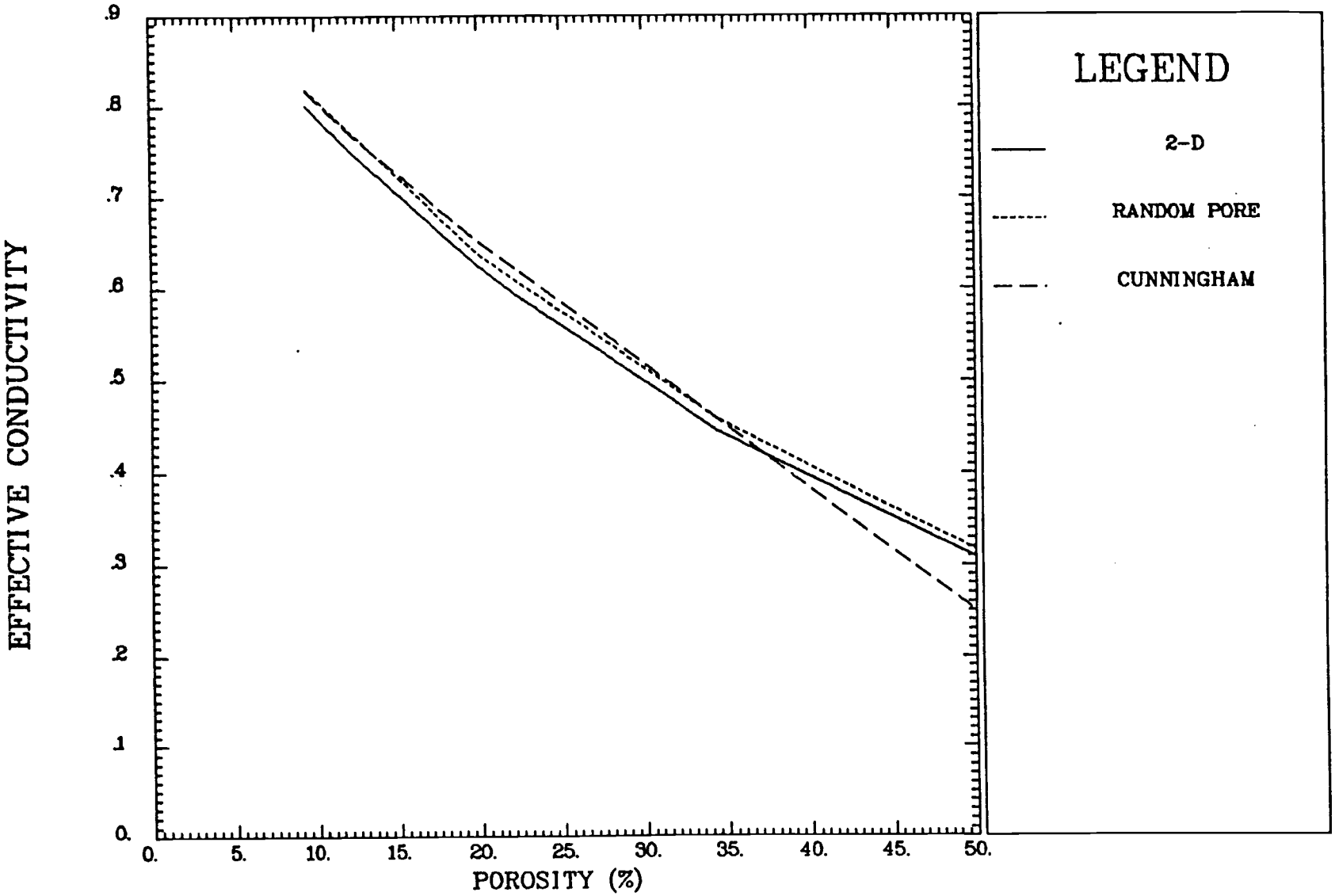

BIBLIOGRAPHY

1. Russell, L. E., "The Structure and Properties of U-C and (U-Pu)C Alloys," New Nuclear Materials Including Non-Metalic Fuels, vol. 1, p. 424, 1963.

2. Chang, S. C., and Vachon, R. I., "The Prediction of the Thermal Conductivity of Two and Three Phase Solid Heterogeneous Mixtures," International Journal of Heat and Mass Transfer, vol. 12, p. 249, 1969.

3. Kampf, H., and Karsten, G., "Effects of Different Types of Void Volumes on the Radial Temperature Distribution of Fuel Pins," Nuclear Applied Technology, vol. 9, p. 288, 1970.

4. Peddicord, K. L., "An Analytical Porosity Correction of Conductivity Based on Spherical Pore Geometry," Transactions of American Nuclear Society, vol. 24, p. 376, 1976.

5. Cunningham, M. E., "Temperature Profiles of Spheres Packed in Regular Arrays," Thesis submitted for Master of Science Degree, Dept. of Nuclear Engineering, Oregon State University, Corvallis, Oregon, 1977.

6. Pierce, B. L., "TAP-A, A Program for Computing Transient or Steady State Temperature Distributions," Westinghouse Astronuclear Laboratory, WANL-TME-1872, December, 1969.

7. Olander, D. R., Fundamental Aspects of Nuclear Reactor Fuel Elements, Technical Information Center, U. S. Department of Energy, TID-26711-P1, pp. 265-267, 1976.

APPENDICES

APPENDIX A

SOLUTION TO THE GOVERNING DIFFERENTIAL EQUATION

The steady state temperature distribution is determined by the well known Laplace Equation

$$\nabla^2 T\ (r,\theta) = 0. \tag{A-1}$$

This can be written in polar coordinates as

$$\frac{1}{r}\frac{\partial}{\partial r}\left(r\frac{\partial}{\partial r} T\ (r,\theta)\right) + \frac{1}{r^2}\frac{\partial^2}{\partial \theta^2} T\ (r,\theta) = 0. \tag{A-2}$$

In order to solve Equation (A-2), it is possible to use the separation of variables technique; that is, assume

$$T\ (r,\theta) = R\ (r)\ \phi\ (\theta).$$

Substituting this expression into Equation (A-2), and multiplying through by r^2 leaves

$$\frac{1}{R(r)} r \frac{d}{dr}\left(r\frac{d}{dr} R\ (r)\right) = -\frac{1}{\phi(\theta)}\frac{d^2}{d\theta^2}\phi\ (\theta). \tag{A-3}$$

Since both sides are in terms of one variable, and set equal to each other, they must be equal to a constant, λ^2. It is now possible to treat each side of the equation individually.

First, the right hand side

$$-\frac{1}{\phi(\theta)}\frac{d^2}{d\theta^2}\phi(\theta) = \lambda^2$$

can be written as

$$\frac{d^2}{d\theta^2}\phi(\theta) + \lambda^2\ \phi(\theta) = 0. \tag{A-4}$$

Equations of this type are well known and have as the solution

$$\phi(\theta) = Bn \sin(\lambda\theta) + An \cos(\lambda\theta) \tag{A-5}$$

where An and Bn are arbitrary constants dependent on the boundary conditions.

The left hand side also reduces to a well documented solution. Expanding

$$r \frac{d}{dr}\left(r \frac{d}{dr} R(r)\right) - \lambda^2 R(r) = 0$$

yields a standard Euler Equation

$$r^2 \frac{d^2}{dr^2} R(r) + r \frac{d}{dr} R(r) - \lambda^2 R(r) = 0 \tag{A-6}$$

which has solutions

$$R(r) = k_1 r^{\lambda} + k_2 r^{-\lambda} \tag{A-7}$$

where k_1 and k_2 are arbitrary constants which are determined by the boundary conditions.

So far, the solutions have depended on λ^2 being greater than zero. Setting $\lambda^2 = 0$ in Equation (A-6) gives

$$r^2 \frac{d^2}{dr^2} R(r) + r \frac{d}{dr} R(r) = 0.$$

Dividing by r^2, and integrating twice gives

$$R(r) = Ao + Bo \ln r. \tag{A-8}$$

Setting $\lambda^2 = 0$ in Equation (A-4) gives

$$\frac{d^2}{d\theta^2} \phi(\theta) = 0$$

which has solutions

$$\phi(\theta) = C_1 + C_2\ \theta.$$

The constant, C_2, must be zero to satisfy the boundary condition that $\phi(\theta)$ be periodic in θ. This condition ensures that $T(r,\theta)$ will be single valued at each point. This leaves C_1, which can be absorbed into A_o. The general solution is the sum of the $\lambda^2 = 0$ and $\lambda^2 \neq 0$ solutions given as

$$T\ (r,\theta) = Ao + Bo\ \ln\ r + \sum_{n=1}^{\infty} \left(k_1\ r^{\lambda n} + k_2\ r^{-\lambda n} \right)\left(Bn\ \sin\ (\lambda_n \theta) + An\ \cos(\lambda_n \theta) \right). \qquad \text{(A-9)}$$

The adiabatic heat flow condition in the cell requires the derivative, $\frac{d}{d\theta} T\ (r,\theta)$ to be zero for $\theta = 0$, and $\theta = \pi$, hence the sine terms must vanish, and $B_n = 0$. For $\theta = \pi$, the only way to satisfy the boundary condition is for λ to be an integer, and equal to n. This yields the general solution

$$T\ (r,\theta) = Ao + Bo\ \ln\ r + \sum_{n=1}^{\infty} \left(An\ r^{n} + Bn\ r^{-n} \right) \cos(n\theta). \qquad \text{(A-10)}$$

To see that this is indeed the general solution, it is only necessary to substitute Equation (A-10) into the governing differential Equation (A-2). When this is done, the first term becomes

$$\sum_{n=1}^{\infty} \left(An\ r^{n-2} + Bn\ r^{-n-2} \right) n^2\ \cos(n\theta)$$

and the second term becomes

$$-\ \sum_{n=1}^{\infty} \left(An\ r^{n-2} + Bn\ r^{-n-2} \right) n^2\ \cos(n\theta).$$

Hence, the equation is satisfied.

APPENDIX B

SOLUTION TO THE ADIABATIC BOUNDARY CONDITION

The cylindrical coordinate system has as its unit vectors $\hat{e}_r$ and and $\hat{e}_\theta$, while the adiabatic condition on the right hand side of the unit cell, Figure 15 is given as

$$\hat{e}_x \cdot q''(r,\theta) = 0 \tag{B-1}$$

where $\hat{e}_x$ = unit vector in the x-direction, $q''(r,\theta)$ = heat flux. It is, therefore, necessary to find a relation between e_x, e_y, and $\hat{e}_r$, $\hat{e}\theta$. Figure 15 illustrates the relationships of the quantities. It is seen that the following is true:

$$\hat{e}_r = \cos \Psi \, \hat{e}_x + \sin \Psi \, \hat{e}_y \tag{B-2}$$

$$\hat{e}_\theta = \cos \theta \, \hat{e}_x - \sin \theta \, \hat{e}_y \tag{B-3}$$

where $\Psi = \left(\frac{\pi}{2} - \theta\right)$

Using the relations

$$\cos\left(\frac{\pi}{2} - \theta\right) = \sin \theta$$

$$\sin\left(\frac{\pi}{2} - \theta\right) = \cos \theta$$

gives the following expressions:

$$\hat{e}_r = \hat{e}_x \sin \theta + \hat{e}_y \cos \theta \tag{B-4}$$

$$\hat{e}_\theta = \hat{e}_x \cos \theta - \hat{e}_y \sin \theta. \tag{B-5}$$

The adiabatic condition is valid only in the range where $\frac{\pi}{4} \leq \theta \leq \frac{3\pi}{4}$. In this range, $r = \frac{L}{2\sin\theta}$ and

$$\hat{e}_x \cdot q''(r,\theta) = 0 \quad \Big| \quad r = \frac{L}{2\sin\theta} \tag{B-6}$$

where

$$q''(r,\theta) = -K^{(2)} \nabla T^{(2)}(r,\theta).$$

Using the definition of the gradient operator in cylindrical coordinates, this expression expands to the following

$$q''(r,\theta) = -K^{(2)} \left(\hat{e}_r \frac{\partial}{\partial r} T^{(2)}(r,\theta) + \hat{e}_\theta \frac{1}{r} \frac{\partial}{\partial \theta} T^{(2)}(r,\theta) \right).$$

Substituting in the expressions for $\hat{e}_r$ and $\hat{e}_\theta$ yields

$$q''(r,\theta) = -K^{(2)} \Big((\hat{e}_x \sin\theta + \hat{e}_y \cos\theta) \frac{\partial}{\partial r} T^{(2)}(r,\theta) + (\hat{e}_x \cos\theta - \hat{e}_y \sin\theta) \frac{1}{r} \frac{\partial}{\partial \theta} T^{(2)}(r,\theta) \Big). \tag{B-7}$$

FIGURE 15.
VECTOR RELATIONSHIPS OF THE UNIT CELL

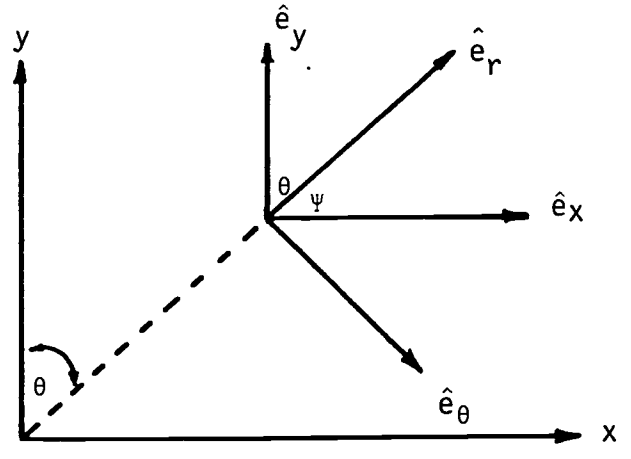

Computing the dot product with $\hat{e}_x$ to give the adiabatic condition gives

$$0 = \hat{e}_x \left(-K^{(2)} \left((\hat{e}_x \sin\theta + \hat{e}_y \cos\theta) \frac{\partial}{\partial r} T^{(2)}(r,\theta) + (\hat{e}_x \cos\theta - \hat{e}_y \sin\theta) \frac{1}{r} \frac{\partial}{\partial \theta} T^{(2)}(r,\theta) \right) \right). \tag{B-8}$$

Using the relations

$$\hat{e}_x \cdot \hat{e}_x = 1$$

and

$$\hat{e}_x \cdot \hat{e}_y = 0$$

reduces the equation to

$$-K^{(2)} \left(\sin\theta \frac{\partial}{\partial r} T^{(2)}(r,\theta) + \cos\theta \frac{1}{r} \frac{\partial}{\partial \theta} T^{(2)}(r,\theta) \right) = 0.$$

Finally, the adiabatic edge condition becomes

$$\sin\theta \frac{\partial}{\partial r} T^{(2)}(r,\theta) + \frac{1}{r} \cos\theta \frac{\partial}{\partial \theta} T^{(2)}(r,\theta) = 0. \tag{B-9}$$

APPENDIX C

ONE-DIMENSION HEAT FLOW ANALYSIS

One-dimensional heat flow allows no heat flow around the pore. Effectively, the pore blocks the heat flow through a projection of its area on the bottom face of the cell. Figure 16 illustrates this. For the case when the thermal conductivity of the pore is very much less than the thermal conductivity of the solid (as in gas pores in ceramic nuclear fuels), the following relationship is observed

$$f(p) \cong 1 - Pc \qquad \text{(C-1)}$$

where Pc is the fractional area of the pore projected on the bottom face of the cell and is given by

$$Pc = \frac{A_{Pore}}{A_{Cell}} = \frac{2RL}{L^2} = \frac{2R}{L} . \qquad \text{(C-2)}$$

The fractional porosity of the cell is equal to the fractional volume occupied by the pore and is given by

$$P = \frac{V_{Pore}}{V_{Cell}} = \frac{\pi R^2 L}{L^3} = \pi\left(\frac{R}{L}\right)^2 . \qquad \text{(C-3)}$$

Rearranging gives

$$\frac{P}{\pi} = \left(\frac{R}{L}\right)^2$$

or

$$\frac{R}{L} = \left(\frac{P}{\pi}\right)^{1/2} . \qquad \text{(C-4)}$$

FIGURE 16.
CELL ORIENTATION FOR ONE-DIMENSIONAL
HEAT FLOW ANALYSIS

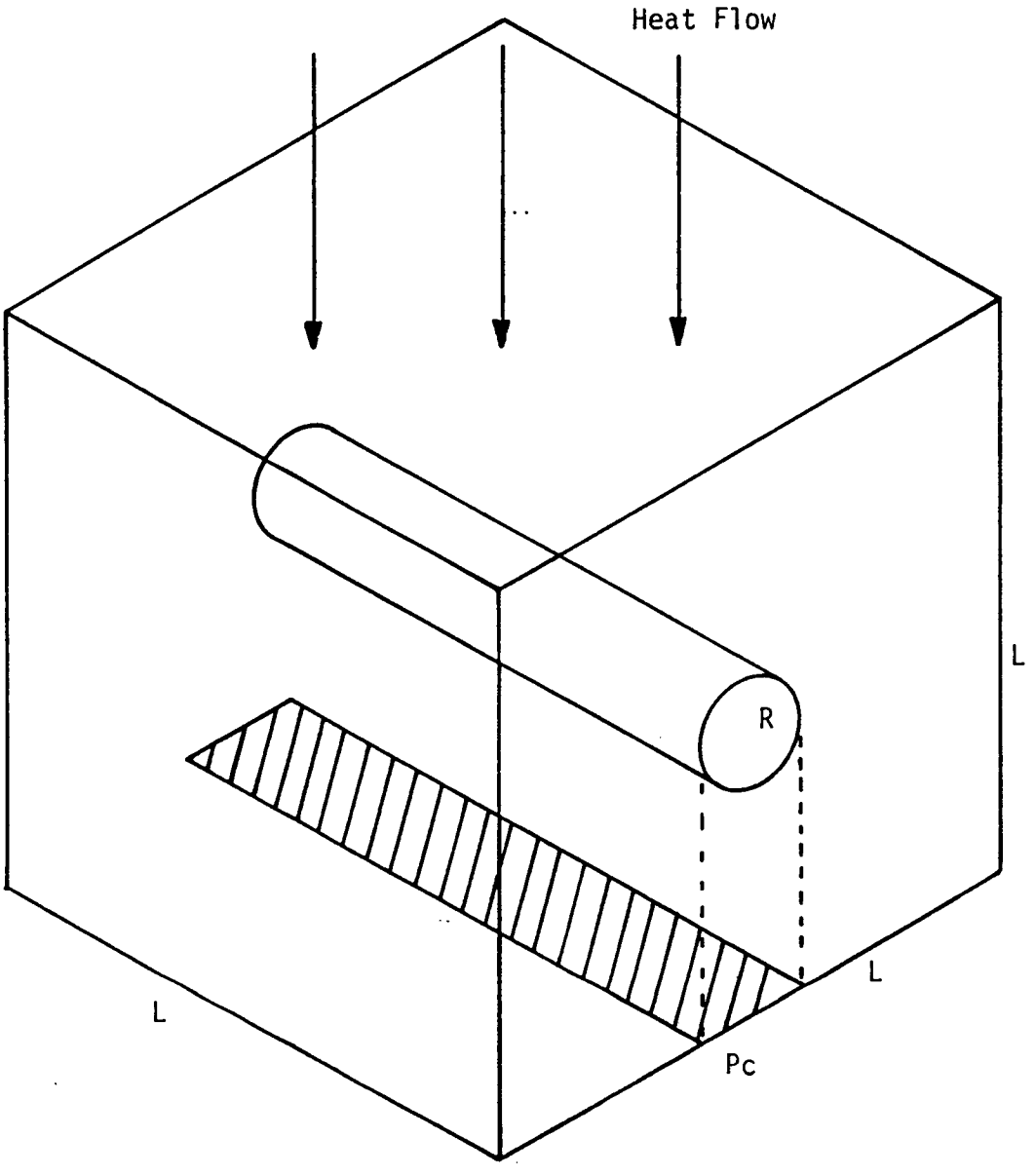

Substituting this expression into Equation (C-2) gives

$$Pc = 2\left(\frac{P}{\pi}\right)^{1/2} . \qquad (C\text{-}5)$$

Substituting this expression into Equation (C-1) yields the final result

$$f(p) = 1 - \frac{2P^{1/2}}{\pi^{1/2}} . \qquad (C\text{-}6)$$

APPENDIX D

TEMPERATURE DISTRIBUTIONS FOR VARIOUS POROSITIES FOR THE UNIT CELL

The following figures contain the nodal patterns and results for each of the porosities studied in this work. The porosity values are 8.38%, 12.57%, 19.63%, 25.65%, 34.91%, and 50.27%. Figures 17 to 22 are the results for the TAP-A data. Figures 23 to 28 are the results for the electrical analog paper. Figures 29 and 34 are the analytical solution results.

FIGURE 17.
TEMPERATURE DISTRIBUTION SOLUTION
FOUND BY FINITE ELEMENT
ANALYSIS (TAP-A) - 8.4% POROSITY

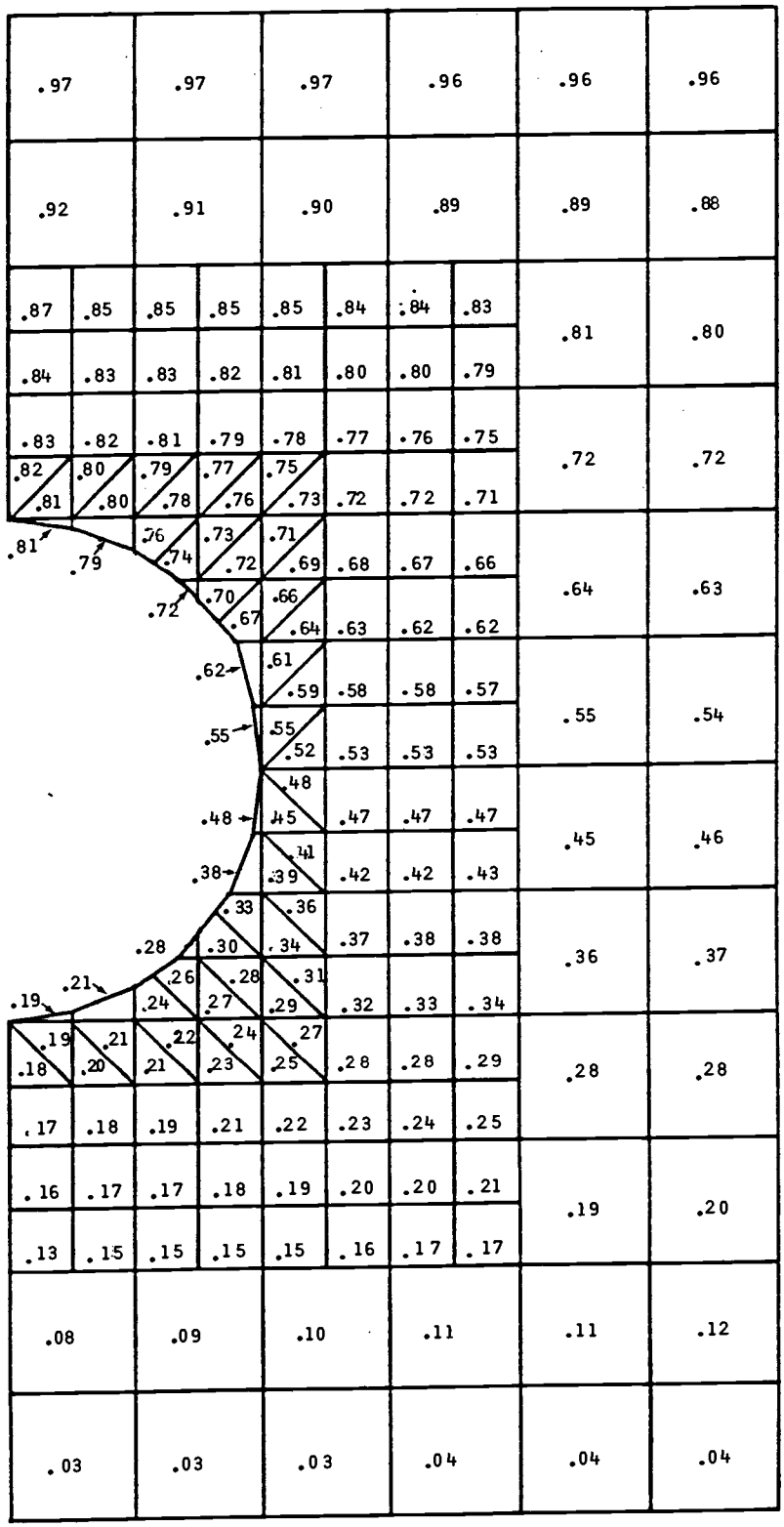

FIGURE 18.
TEMPERATURE DISTRIBUTION
FOUND BY FINITE ELEMENT ANALYSIS
(TAP-A) - 12.6% Porosity

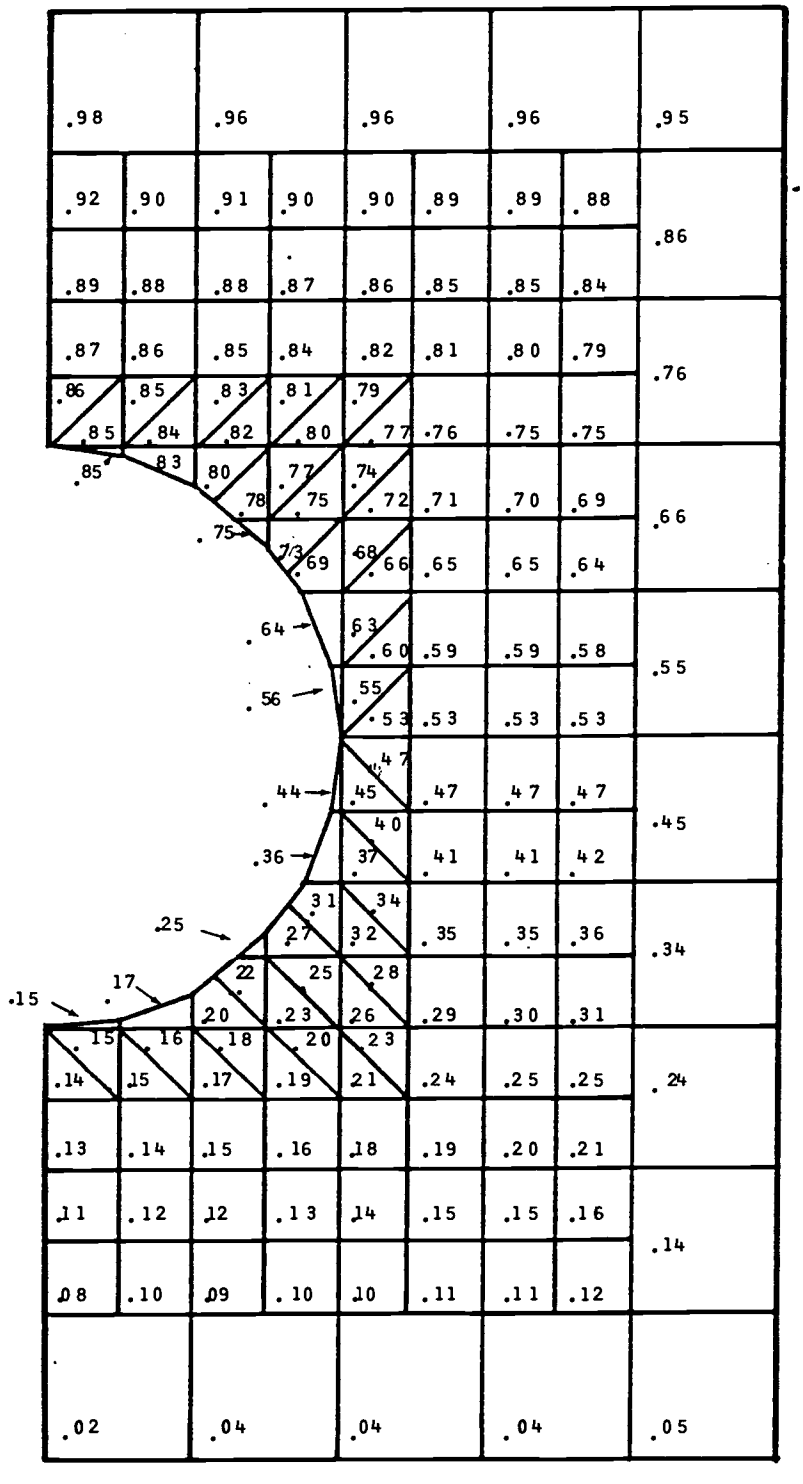

FIGURE 19.
TEMPERATURE DISTRIBUTION SOLUTION
FOUND BY FINITE ELEMENT
ANALYSIS (TAP-A) - 19.6% POROSITY

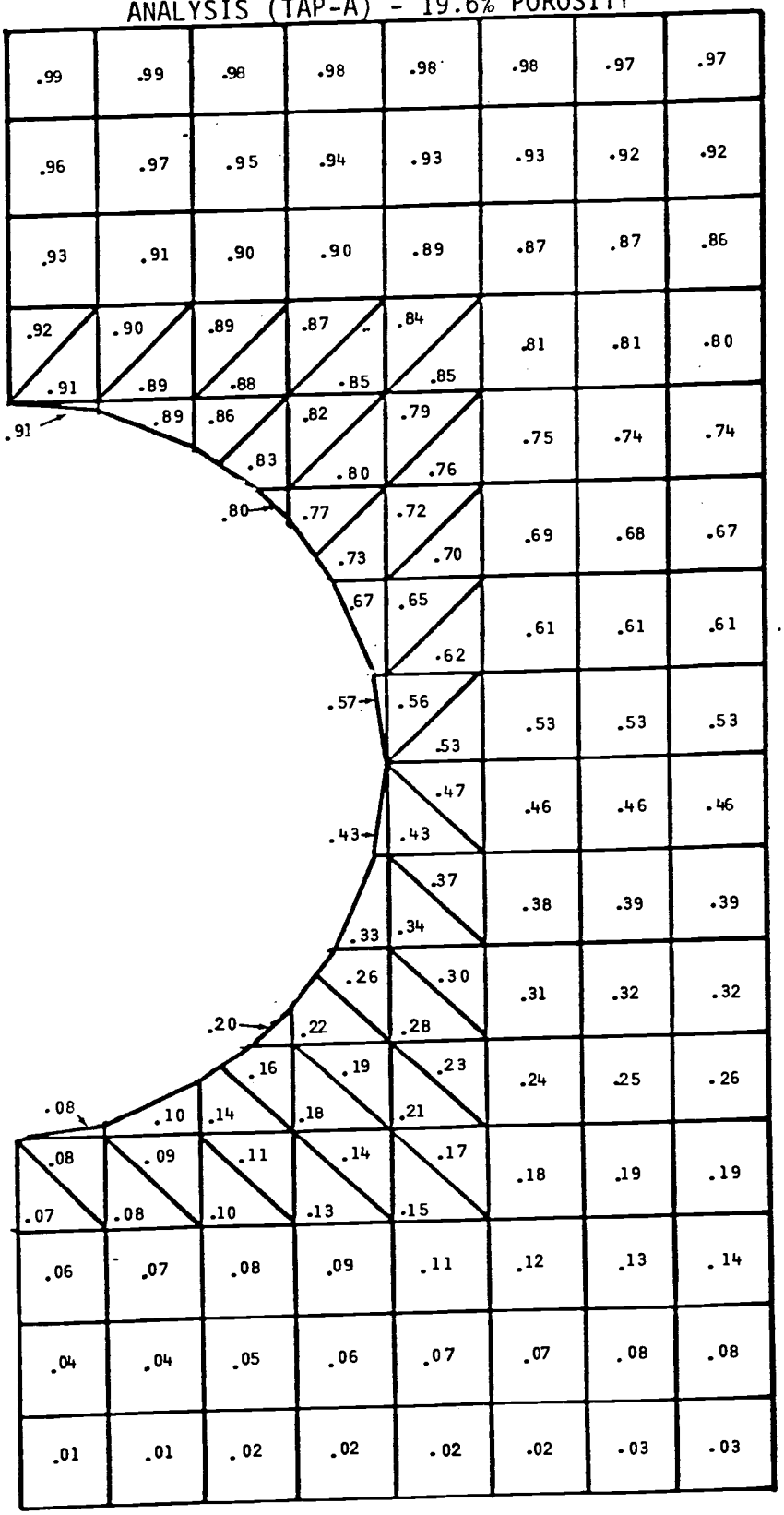

FIGURE 20.
TEMPERATURE DISTRIBUTION SOLUTION
FOUND BY FINITE ELEMENT
ANALYSIS (TAP-A) - 25.6% POROSITY

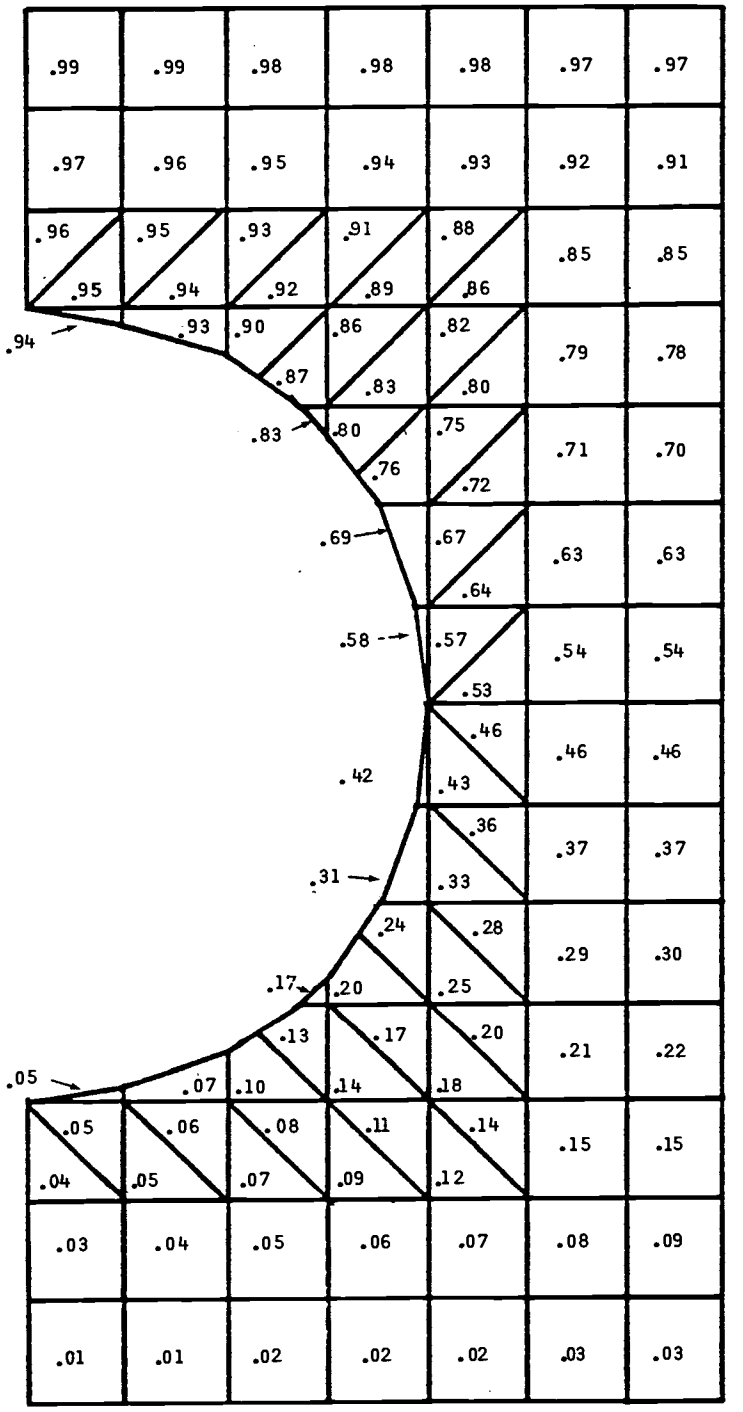

FIGURE 21.
TEMPERATURE DISTRIBUTION
FOUND BY FINITE ELEMENT
ANALYSIS (TAP-A) - 34.9% POROSITY

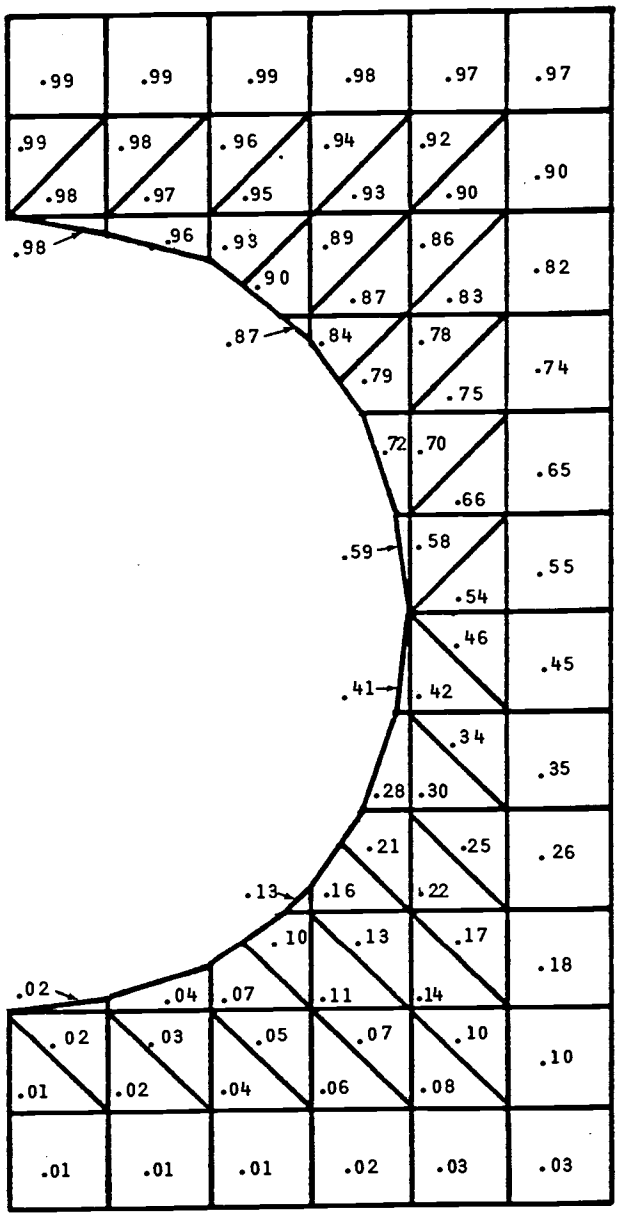

FIGURE 22.
TEMPERATURE DISTRIBUTION
FOUND BY FINITE ELEMENT
ANALYSIS (TAP-A) - 50.3% POROSITY

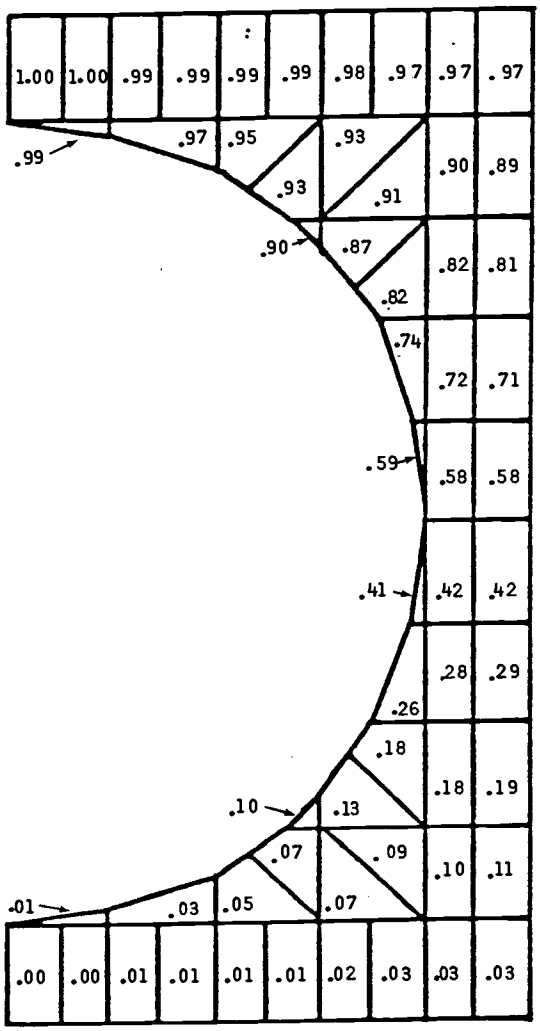

FIGURE 23.
TEMPERATURE DISTRIBUTION SOLUTION
FOUND BY ELECTRICAL ANALOG -
8.4% POROSITY

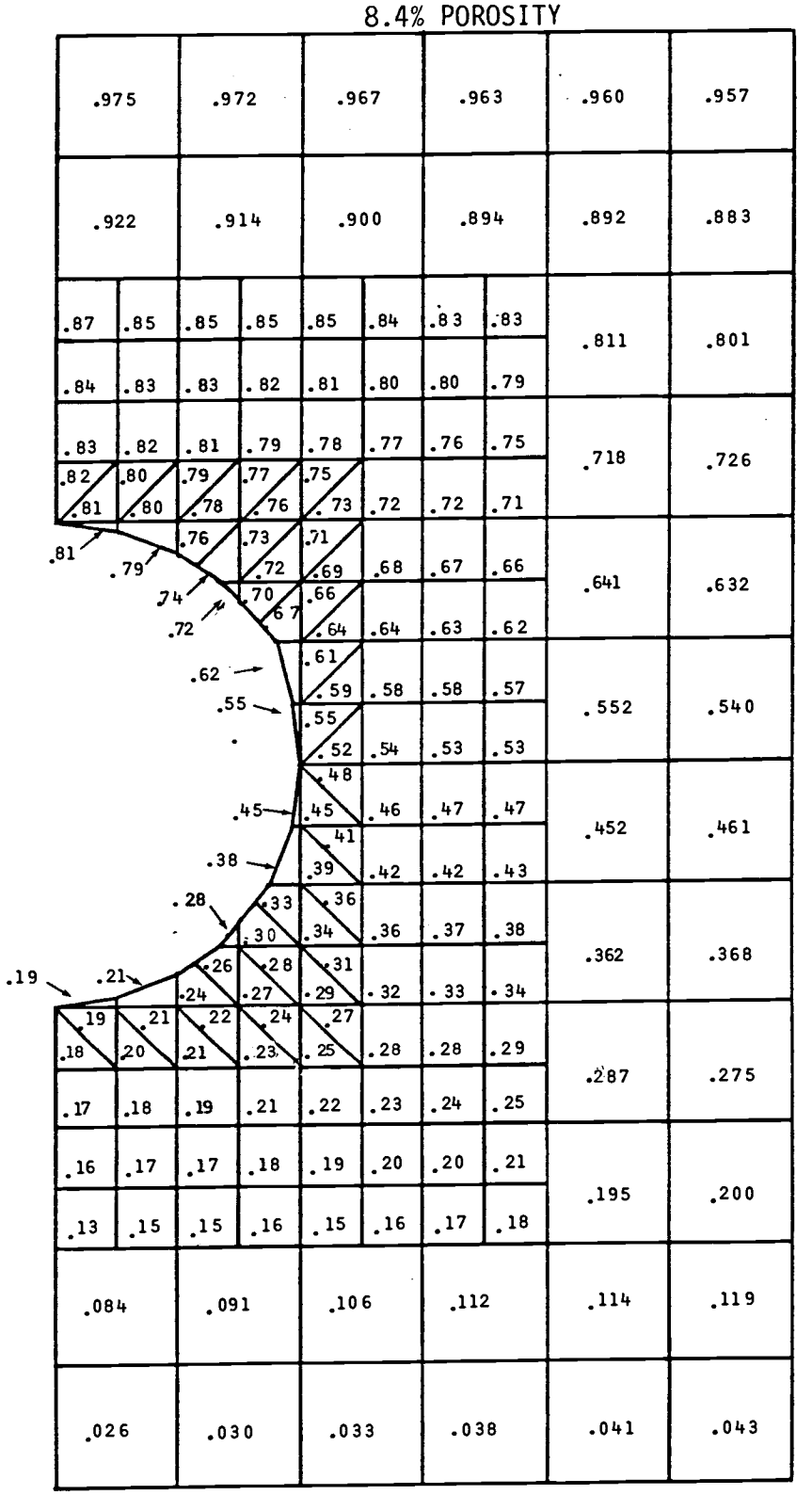

FIGURE 24.
TEMPERATURE DISTRIBUTION SOLUTION
FOUND BY ELECTRICAL ANALOG
12.6% POROSITY

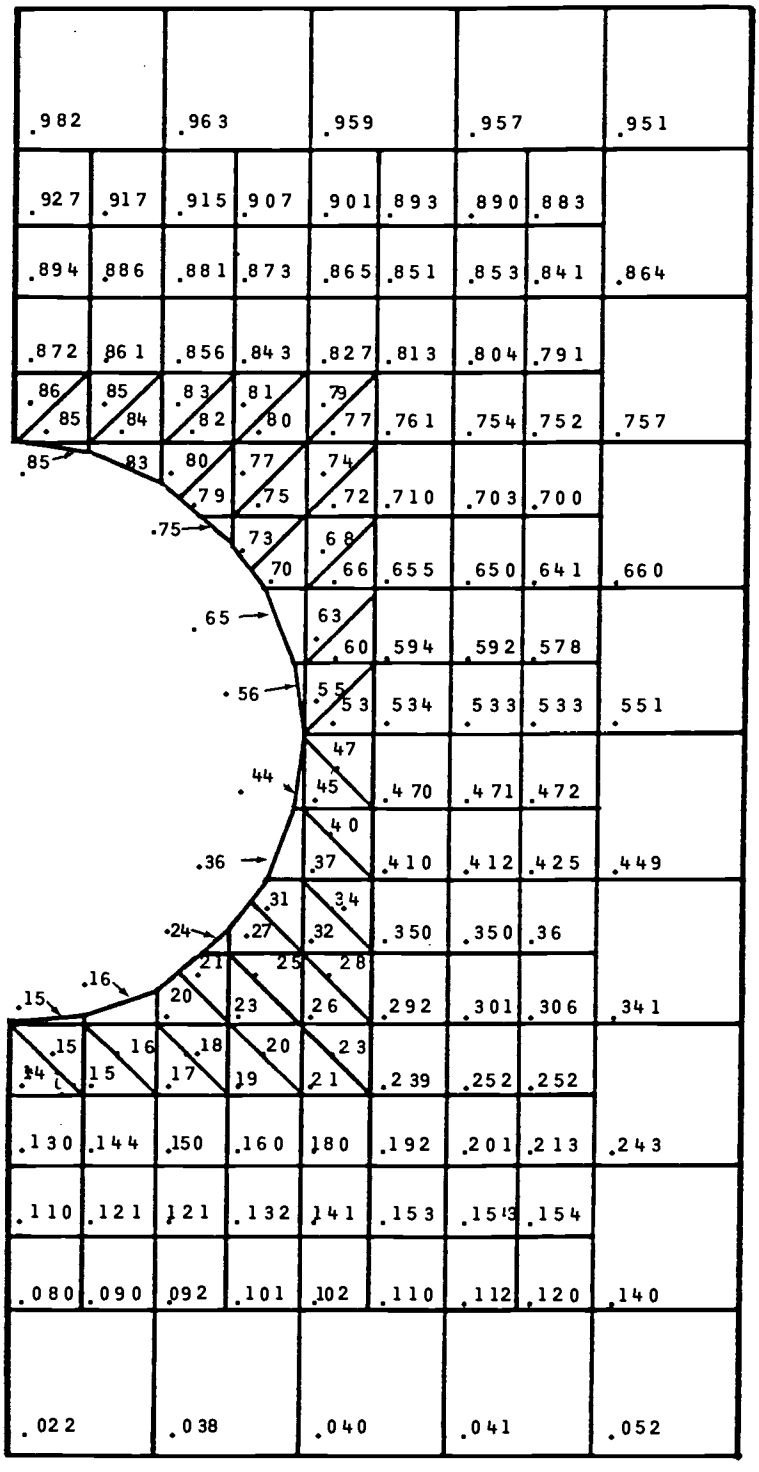

FIGURE 25.
TEMPERATURE DISTRIBUTION SOLUTION
FOUND BY ELECTRICAL ANALOG -
19.6% POROSITY

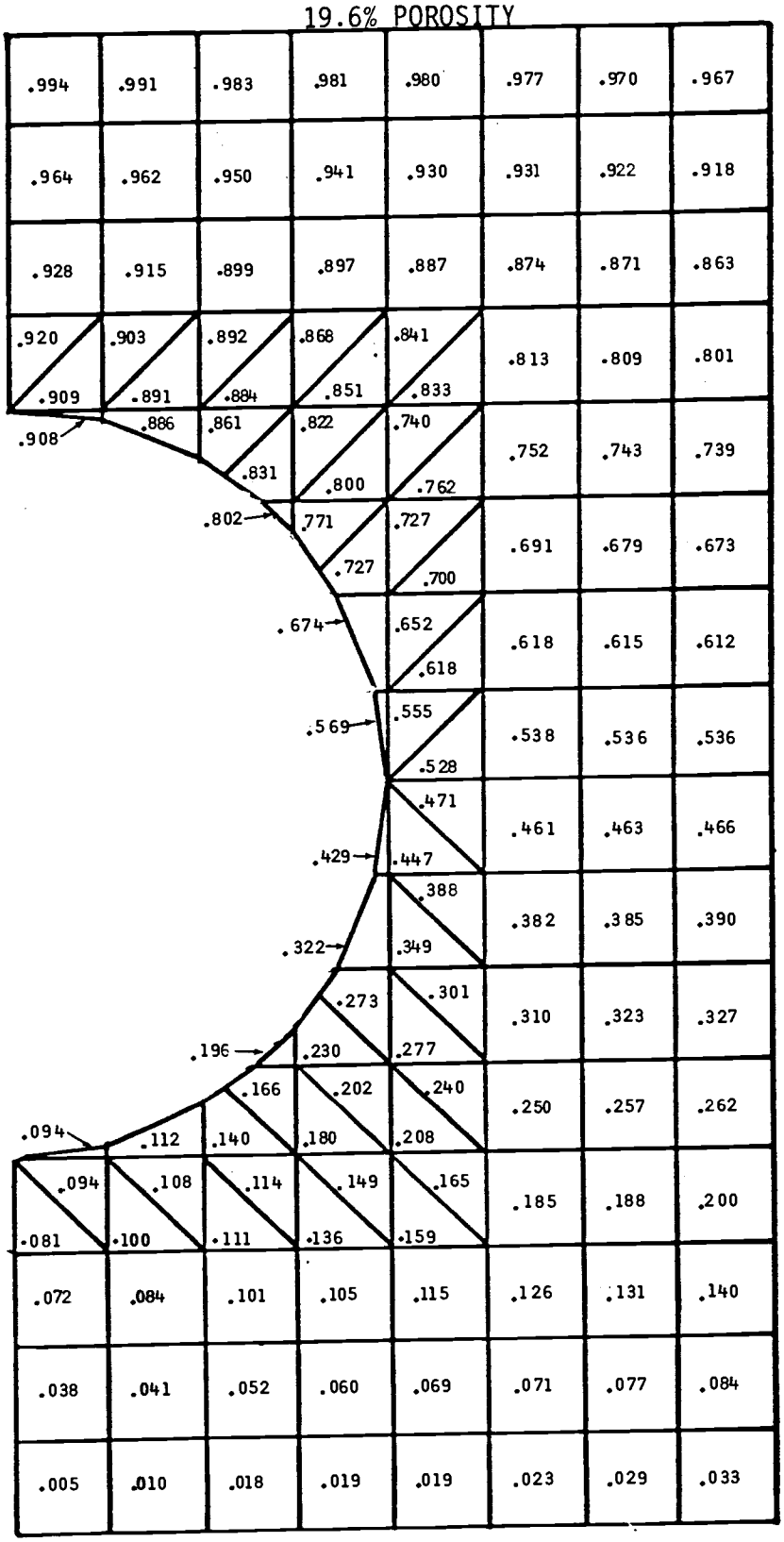

FIGURE 26.
TEMPERATURE DISTRIBUTION SOLUTION
FOUND BY ELECTRICAL ANALOG -
25.6% POROSITY

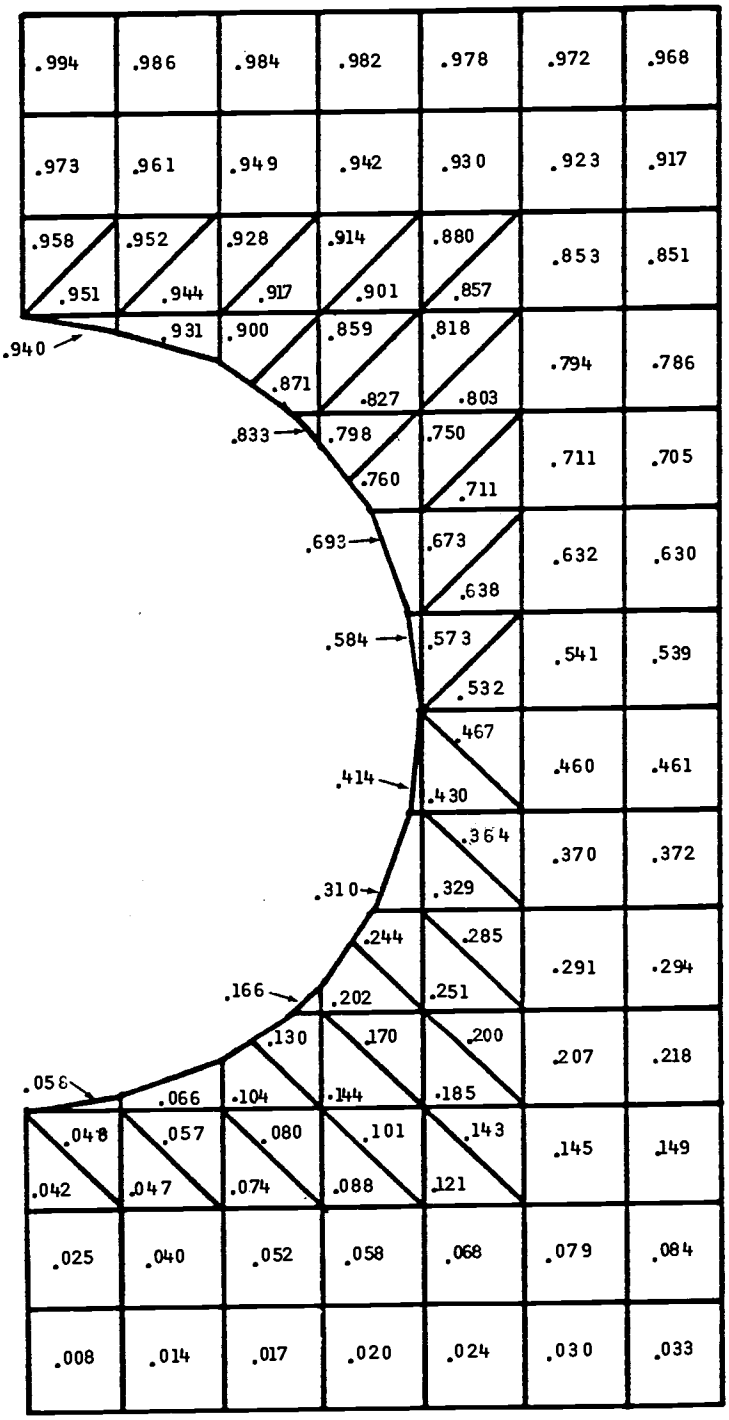

FIGURE 27.
TEMPERATURE DISTRIBUTION
FOUND BY ELECTRICAL ANALOG -
34.9% POROSITY

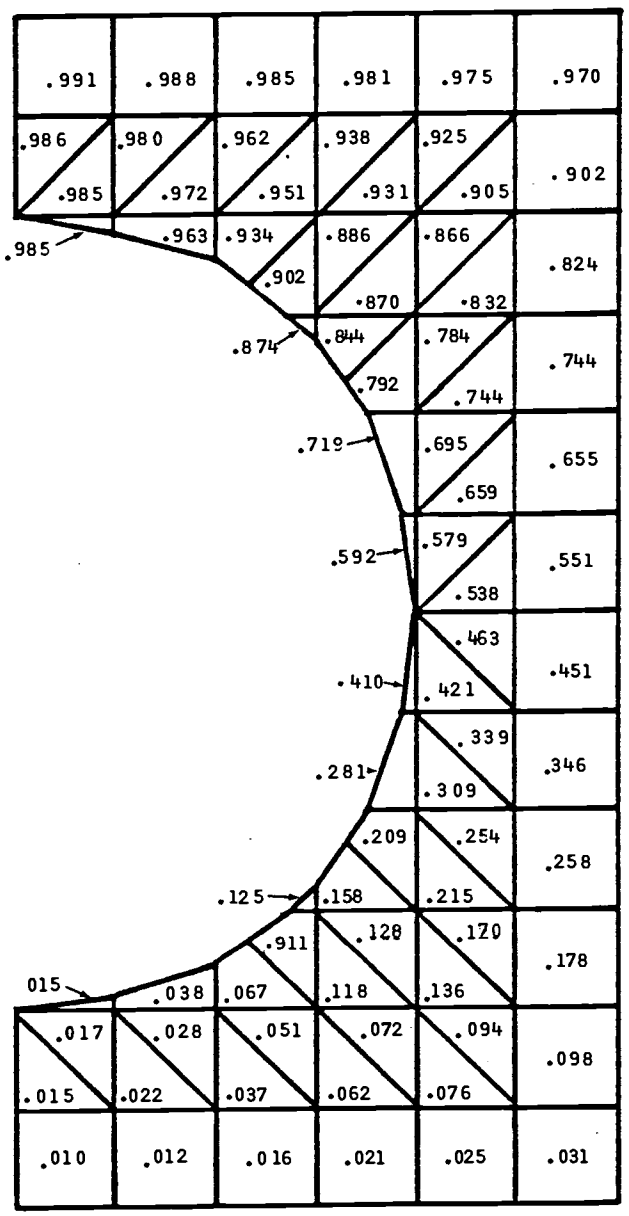

FIGURE 28.
TEMPERATURE DISTRIBUTION
FOUND BY ELECTRICAL ANALOG -
50.3% POROSITY

FIGURE 29.
TEMPERATURE DISTRIBUTION
FOUND BY ANALYTICAL SOLUTION -
8.4% POROSITY

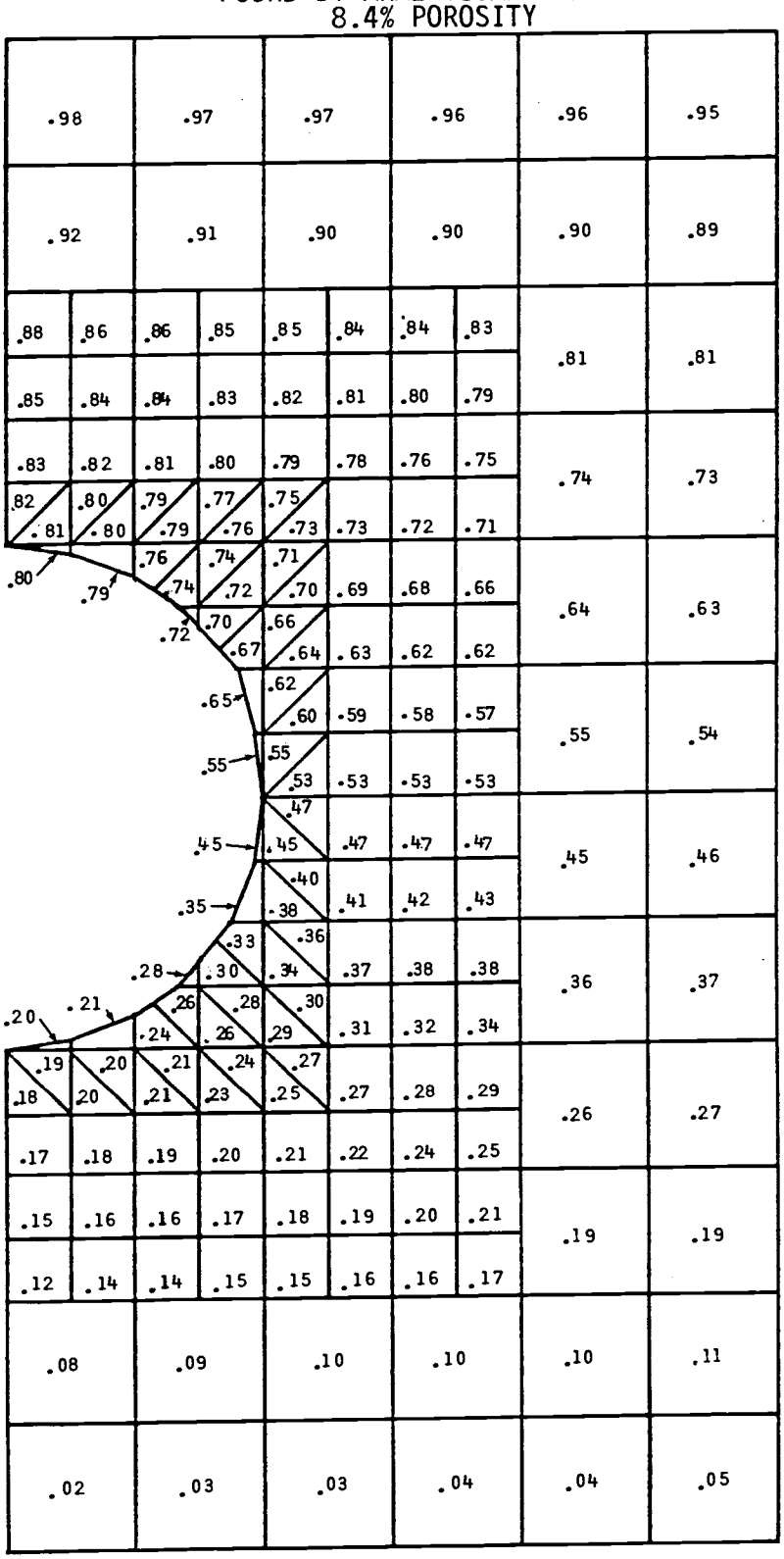

FIGURE 30.

TEMPERATURE DISTRIBUTION
FOUND BY ANALYTICAL SOLUTION -
12.6% POROSITY

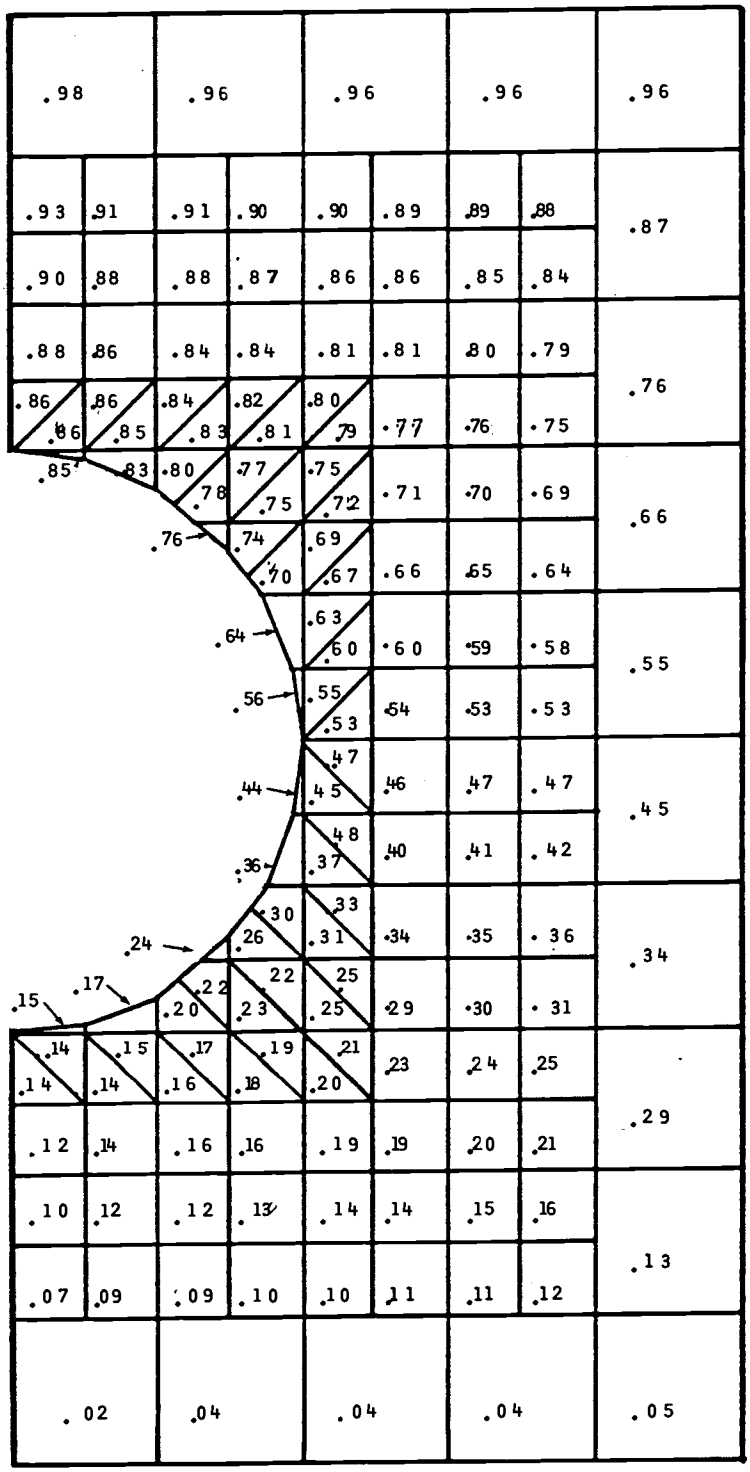

FIGURE 31.
TEMPERATURE DISTRIBUTION FOUND BY
ANALYTICAL SOLUTION - 19.6% POROSITY

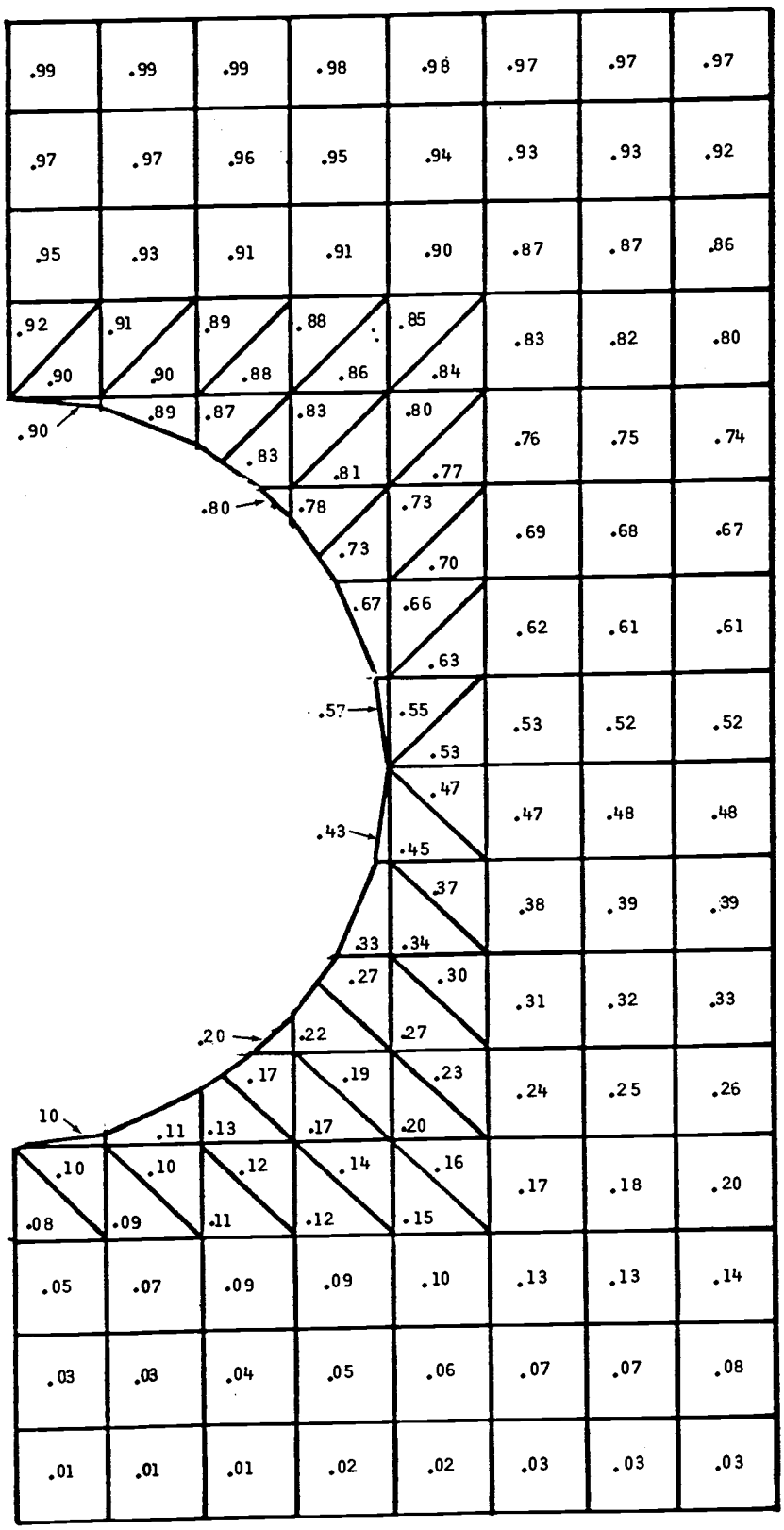

FIGURE 32.
TEMPERATURE DISTRIBUTION
FOUND BY ANALYTICAL SOLUTION -
25.6% POROSITY

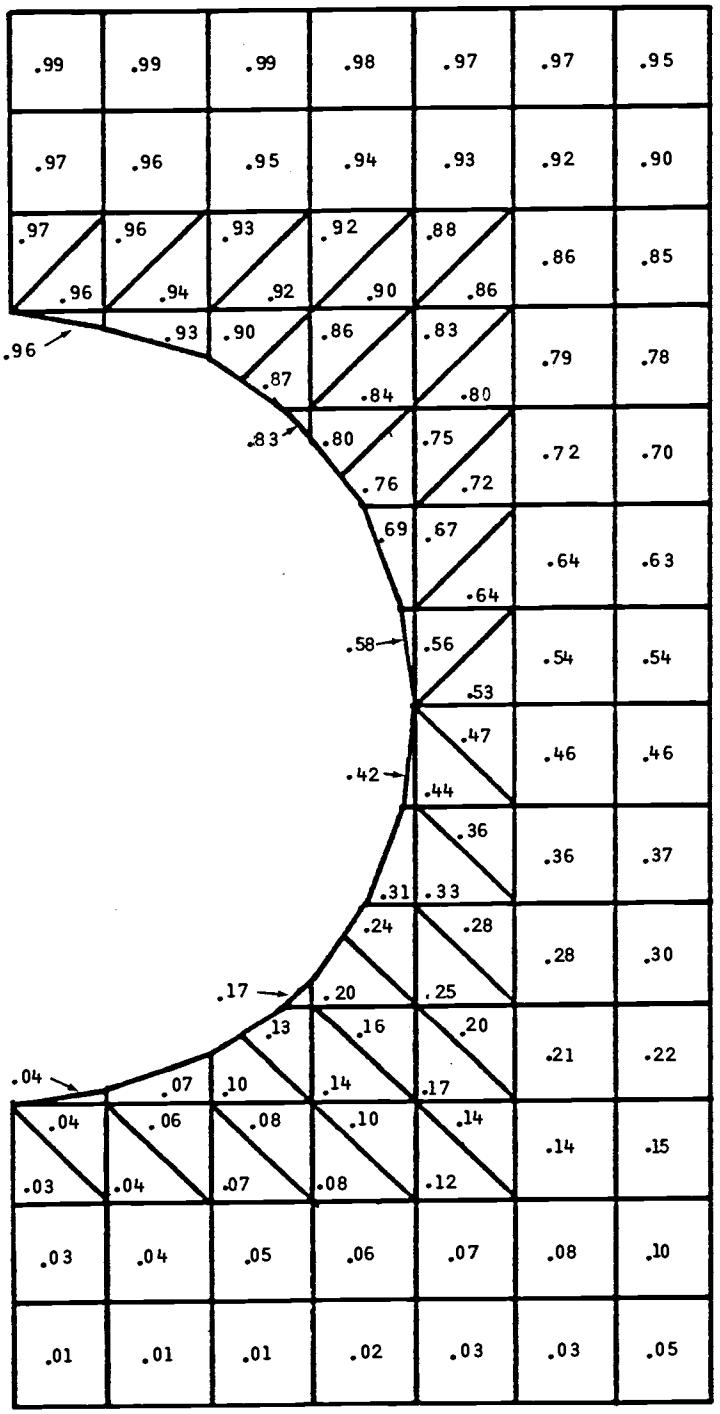

FIGURE 33.
TEMPERATURE DISTRIBUTION FOUND BY
ANALYTICAL SOLUTION - 34.9% POROSITY

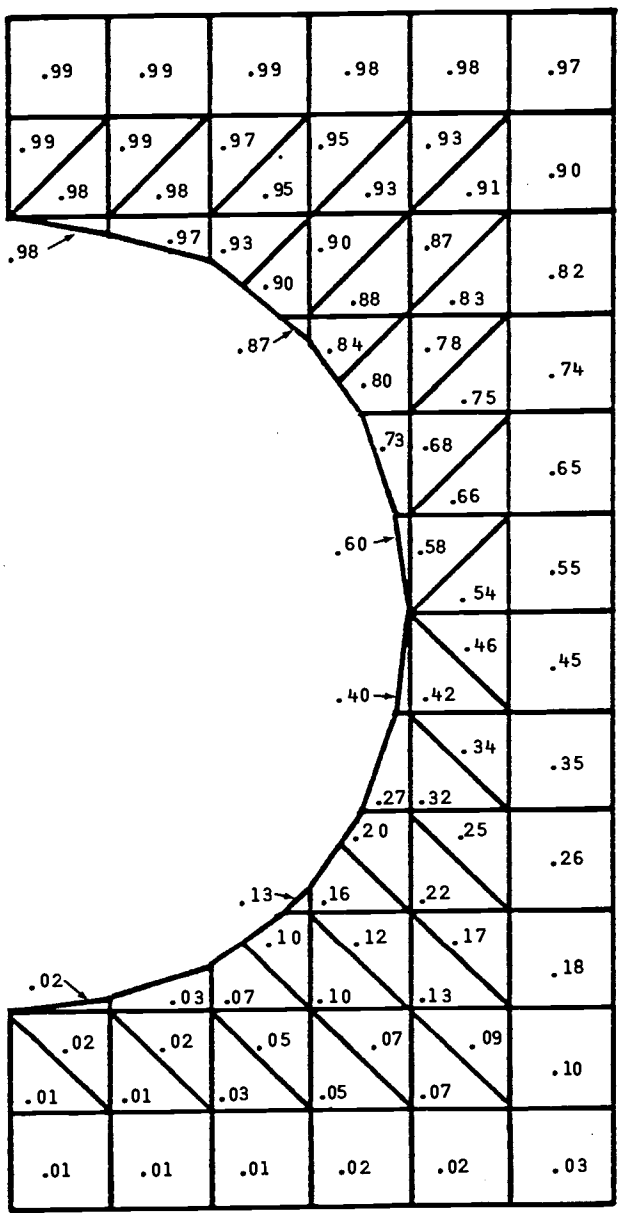

FIGURE 34.
TEMPERATURE DISTRIBUTION
FOUND BY ANALYTICAL SOLUTION -
50.3% POROSITY